DTU Library

An efficient method for estimating the structural stiffness of flexible floating structures

Zhou, Baoshun; Yang, Zhixun; Amini-Afshar, Mostafa; Shao, Yanlin; Bingham, Harry B.

Published in:
Marine Structures

Link to article, DOI:
10.1016/j.marstruc.2023.103527

Publication date:
2024

Document Version
Publisher's PDF, also known as Version of record

Marine Structures 93 (2024) 103527

Contents lists available at ScienceDirect

Marine Structures

journal homepage: www.elsevier.com/locate/marstruc

An efficient method for estimating the structural stiffness of flexible floating structures

Baoshun Zhou [a], Zhixun Yang [b], Mostafa Amini-Afshar [a], Yanlin Shao [a], Harry B. Bingham [a,*]

[a] *Section for Fluid Mechanics, Coastal and Maritime Engineering, Department of Civil and Mechanical Engineering, Technical University of Denmark, 2800, Lyngby, Denmark*

[b] *Institute of Marine Machinery, College of Mechanical and Electrical Engineering, Harbin Engineering University, 150001, No. 145 Nantong Street, Harbin, China*

ARTICLE INFO

Keywords:
Hydroelastic analysis
Ships
Periodic floating structures
Euler–Bernoulli beams
Structural stiffness
Effects of stiffeners

ABSTRACT

In the hydroelastic analysis of large floating structures, the structural and hydrodynamic analyses are coupled, and the structural stiffness plays an important role in the accurate prediction of the response. However, there is usually a large difference between the longitudinal and the cross-sectional scales of modern ships, and the sectional configurations are generally complex, making it difficult to obtain the exact structural stiffness. Using a full finite element model to calculate the structural stiffness is inevitably time-consuming. Since modern ship structures are usually nearly periodic in the longitudinal direction, we treat the hull as a periodic Euler–Bernoulli beam and use a novel implementation of asymptotic homogenization (NIAH) to calculate the effective stiffness. This can greatly improve the computational efficiency compared with a full finite element model. Based on a combination of finite element and finite difference methods, we develop an efficient analysis technique to solve the hydroelastic problem for nearly-periodic floating structures. The finite element method is used to efficiently calculate the structural stiffness, and the finite difference method is used to solve the hydrodynamic problem. This proposed technique is validated through several test cases with both solid and thin-walled sections. A range of representative mid-ship sections for a container ship are then considered to investigate the influence of both transverse and longitudinal stiffeners on the structural deformations. A simple method for including non-periodic end effects is also suggested.

1. Introduction

With the increasing needs of maritime transport, very large floating structures (VLFS) have become more common. In a traditional hydrodynamic analysis, ships are usually regarded as rigid structures, but the increased flexibility of large ships pushes the natural frequencies closer to the wind-wave forcing and leads to larger responses which can no longer be ignored. Over the past several decades, hydroelastic analysis methods have been developed to predict the response of flexible structures [1–10]. Most of these methods treat the ship as a beam model and couple the hydrodynamic and structural analyses. Euler–Bernoulli beam theory [11–13] is the most commonly used structural model, but Timoshenko beam theory [14,15] is also often invoked to include shear effects. The torsional response can also be predicted using a special beam model if necessary. The hydrodynamic calculations are sometimes done using Navier–Stokes equation solvers (CFD) such as OpenFOAM [16], or STAR-CCM+ [17]. However, CFD solvers

* Corresponding author.
E-mail address: hbbi@dtu.dk (H.B. Bingham).

https://doi.org/10.1016/j.marstruc.2023.103527
Received 23 March 2023; Received in revised form 17 July 2023; Accepted 11 October 2023
Available online 1 November 2023

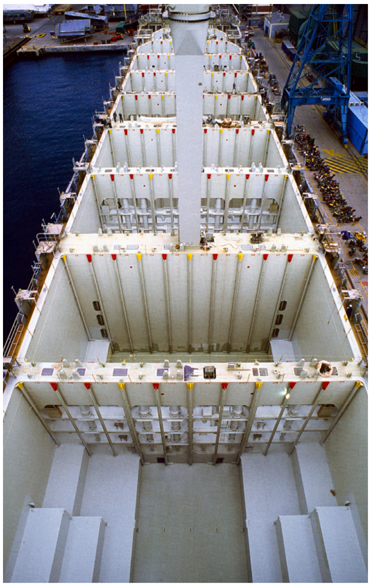

(a) Bird's eye view.

(b) Complex section.

Fig. 1. Examples of modern container ship structures. Fig. 1(a) is from https://commons.wikimedia.org/wiki/File:Containerlader%C3%A4ume_Schiff_retouched.jpg, and Fig. 1(b) is from https://www.bloomberg.com/news/photo-essays/2013-09-05/holy-ship, which both were accessed on March 22 2023.

are extremely time-consuming and limited to a small number of specific operational conditions. Therefore, most solvers are based on potential-flow theory. For example, WAMIT [18–20] and HydroStar [21,22] can efficiently solve the first- and second-order problems at zero forward speed using the Boundary Element Method (BEM). These solvers generally treat hydroelastic problems by means of generalized radiation modes [23].

Over the past two decades, the maritime group at the Technical University of Denmark has developed an open-source finite difference-based hydrodynamic solver, OceanWave3D-Seakeeping [24–26], which also includes generalized modes to solve hydroelastic problems [27–29]. A key component of this solution, representing the coupling between the structural and the hydrodynamic problems, is the structural stiffness matrix. It is a non-trivial task to accurately estimate the global structural stiffness of a large ship, due to the large range of scales associated with the details of a sectional girder and the length of the ship. These days, a full finite element method (FEM) model is often developed for a new ship design using commercial software such as NASTRAN [30], ABAQUS [31], or ANSYS [32]. However, generating a full ship model using these tools is very time-consuming and computationally intensive. The model may also fail to converge when the difference between the global and local scales is very large. Fig. 1 shows two examples of the structural layout of real ships. The complexity of the sections is clear, illustrating how difficult it is to model all the details using a finite element method. Considering that many modern ships are usually characterized by a nearly periodic structure in the longitudinal direction, the structural stiffness can be efficiently calculated based on a representative microstructure which is defined as a unit-cell. For example, the ship structure as shown in Fig. 1(a) can be seen to have a nearly periodic characteristic along most of its length, consisting of an array of unit-cell structures.

Several methods have been developed for efficient calculation of the mechanical properties of periodic structures including, the representative volume element (RVE) method [33] and the asymptotic homogenization method (AH) [34,35]. The RVE method can be implemented easily but lacks a solid mathematical foundation, and thus a high calculation accuracy cannot be guaranteed. The AH method, on the other hand, has been derived based on a rigorous mathematical perturbation theory which is able to accurately predict the properties of periodic structures [36]. Therefore, the AH method has been further developed for various applications. For example, many researchers [37–39] have expanded the AH method to calculate the properties of two- and three-dimensional periodic structures. In some studies [40–42], the vibration problem has been efficiently evaluated using the AH method. To predict the properties of one-dimensional periodic structures, the AH method has been further developed by many scholars [43–47]. The AH method was derived using three-dimensional elasticity theory [48] and satisfies the corresponding governing equations. To apply AH to another case, a large amount of coding work and tedious mathematical manipulations must be carried out. To improve the calculation efficiency, Cheng et al. [49] developed a novel implementation of the AH method which is known as NIAH. Cai et al. [50] and Yi et al. [36] modified NIAH to calculate the properties of one-dimensional periodic beams and two-dimensional periodic plates, respectively. Xu et al. [51,52] extended the NIAH to calculate the shear properties of periodic structures. Yan et al. [53,54] used NIAH to analyze the stiffness and stress properties of helically wound structures.

In this paper, we model flexible structures as Euler–Bernoulli beams and develop an efficient strategy to solve for their hydroelastic response to ocean waves. By applying the NIAH method to estimate the global structural stiffness, the computational cost is reduced significantly compared to a full FEM analysis. Based on the estimated structural stiffness, the hydroelastic response is predicted using the linear potential-flow solver OceanWave3D-Seakeeping. The strategy is validated by comparison with benchmark numerical and experimental results for several test cases with both solid-section and thin-walled structures. Finally, we consider several representative mid-ship sections for a container ship and illustrate how the strategy can be used for the loading analysis and structural response of modern ships. Here we discuss the influence of both longitudinal and transverse stiffeners on the hydroelastic response in the vertical bending modes. We also propose a simple method for including the non-periodic end effects.

The rest of this paper unfolds as follows. Section 2 describes a common workflow of the hydroelastic analysis of flexible bodies. In Section 3, we introduce the derivation and the FEM implementation of NIAH, and develop an efficient analysis workflow for the hydroelastic problem of periodic floating structures based on NIAH. Section 4 gives a couple of validation cases of solid-section and thin-walled structures. Section 5 studies the hydroelastic problem of open-section models for a container ship. Section 6 concludes this paper.

2. Hydroelastic analysis workflow

In this section, based on Newman's work [23], we briefly outline the common analysis workflow for predicting the hydroelastic response of flexible structures. We adopt the eigenmodes of an Euler–Bernoulli beam to represent the generalized motion modes of the ship, and these hydrodynamic problems are solved under the assumptions of linear potential flow theory. The corresponding frequency-domain equations of motion are

$$\sum_{j=1}^{6+N} [-\omega^2(M_{ij} + a_{ij}) + \mathrm{i}\omega b_{ij} + c_{ij} + C_{ij}]\xi_j = X_i, \qquad i = 1,\ 2,\ \ldots,\ 6+N, \tag{1}$$

where i and j denote the force direction and the motion mode, respectively. N denotes the total number of flexible modes, ω is the incident wave forcing radian frequency and the response is assumed to be time-harmonic so that $x_j(t) = \Re\{\xi_j\, \mathrm{e}^{\mathrm{i}\omega t}\}$ with $\mathrm{i} = \sqrt{-1}$ the imaginary unit. M_{ij} and C_{ij} are inertial mass and structural stiffness coefficients respectively, which can be calculated from

$$M_{ij} = \int_{-L/2}^{L/2} m h_i^z(x) h_j^z(x) dx, \tag{2}$$

and

$$C_{ij} = \int_{-L/2}^{L/2} EI h_i^{z''}(x) h_j^{z''}(x) dx. \tag{3}$$

Here h_i^z is the vertical displacement defined by the i^{th} mode shape of an Euler–Bernoulli beam, which is defined below. In Eqs. (2) and (3), m and EI are the distributed mass and the bending stiffness, respectively. In this paper, the distributed mass is assumed to be uniform along the length of the ship, which can be calculated with ease once the draft is known. The bending stiffness EI is also assumed to be constant along the ship length. The shape functions of the Euler–Bernoulli beam are given by

$$\begin{cases} h_{2j+5}^z(p) = \frac{1}{2}\left(\frac{\cos\kappa_{2j-1}p}{\cos\kappa_{2j-1}} + \frac{\cosh\kappa_{2j-1}p}{\cosh\kappa_{2j-1}}\right), & j = 1,2,\ldots \\ h_{2j+6}^z(p) = \frac{1}{2}\left(\frac{\sin\kappa_{2j}p}{\sin\kappa_{2j}} + \frac{\sinh\kappa_{2j}p}{\sinh\kappa_{2j}}\right), & j = 1,2,\ldots \end{cases} \tag{4}$$

where κ_j is the natural wavenumber in eigenmode j and $p = 2x/L$ is the coordinate normalized by the ship length L. κ_j satisfies the equation

$$(-1)^j \tan\kappa_j + \tanh\kappa_j = 0, \tag{5}$$

and the first four roots are

$$\kappa_2 = 2.3650, \qquad \kappa_3 = 3.9266, \qquad \kappa_4 = 5.4978, \qquad \kappa_5 = 7.0686. \tag{6}$$

In Eq. (3), $h_i^{z''}$ is the second derivative of the mode shape with respect to its argument. The corresponding shape functions for heave, pitch and the first four vertical bending modes are shown in Fig. 2. In Eq. (1), a_{ij}, b_{ij} and X_i are the hydrodynamic coefficients, i.e. the added mass, damping and excitation force coefficients, and ξ_j is the motion response phasor in mode j.

The development of the hydrodynamic solution based on linear potential flow theory, is very mature at this point, although there are still several unresolved issues when the vessel has non-zero forward speed. Relatively few hydroelastic solutions at forward speed are available in the literature, and experimental measurements are also relatively sparse. In this paper, we use a finite difference method to solve the hydrodynamic problem, and a detailed description of this solution can be found in Refs. [24,25,28]. As mentioned by Newman in [23] the total hydrostatic stiffness includes both gravitational and buoyancy contributions.

To complete the solution of Eq. (1), we need an accurate estimate of the bending stiffness for the ship hull, but that is not an easy task. For periodic floating structures, we take a homogenization approach to estimate the equivalent bending stiffness. According to solid mechanics theory [55], the homogenized bending stiffness of all sections can be expressed by

$$EI_y = \frac{1}{L}\int_L \iint_A Ez^2 dS\, dx, \tag{7}$$

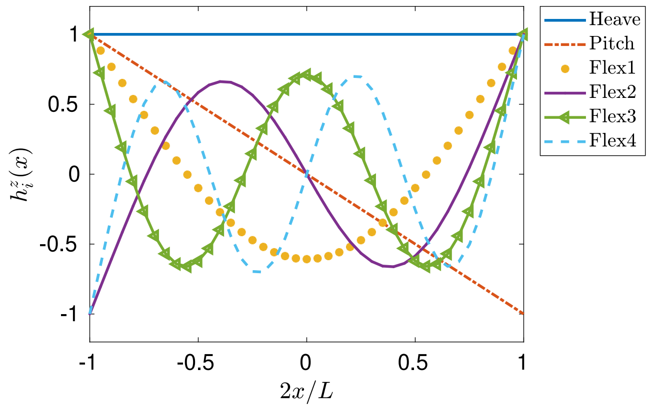

Fig. 2. Shape functions for heave, pitch and the first four vertical bending modes.

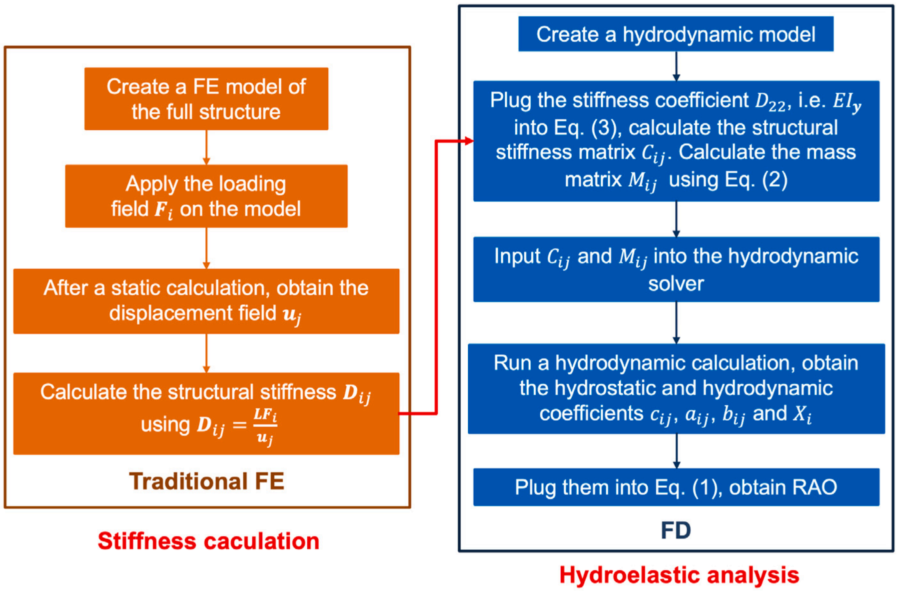

Fig. 3. A standard workflow for the hydroelastic analysis. F_i represents the applied force in direction i from displacement u_j in mode j. For example, to solve the bending stiffness D_{22} which is used on the right-hand side, F_2, u_2 are the bending moment and the rotation angle around the y axis respectively.

where I_y is the average of the vertical area moment of inertia of all sections, and E is the modulus of elasticity. The sectional area A is a function of x, i.e. $A = A(x)$. The vertical coordinate z is a function of x and y, i.e. $z = z(x, y)$. Exact solutions of Eq. (7) can be used to calculate the bending stiffness of simple sections, but exact solutions are rarely available for real engineering structures. For a ship, the cross sections are usually complex and change along the ship length, and the homogenization calculation of the bending stiffness using Eq. (7) should be done over the whole ship, which is difficult if all geometrical details are included. With the continuous improvement of computing techniques, FEM has been applied to calculate the bending stiffness of engineering structures. In a standard FEM static calculation of the structural stiffness, as shown on the left side of Fig. 3, a full model is usually required. For engineering structures with a large slenderness ratio like ships, the full-size simulation is often very time-consuming and can have convergence issues. Therefore, in the hydroelastic analysis of large floating structures, it is key to find an accurate and efficient way to calculate the structural stiffness.

3. New hydroelastic analysis workflow for periodic floating structures

Considering that modern ships usually have a nearly-periodic longitudinal structure, we introduce a novel implementation of asymptotic homogenization (NIAH) to efficiently calculate the structural stiffness, and develop an efficient scheme for the hydroelastic analysis of large ships.

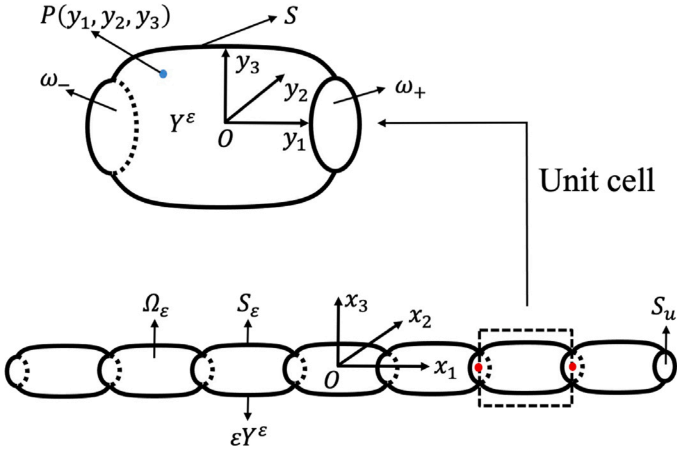

Fig. 4. A one-dimensional periodic structure and the corresponding unit-cell.

3.1. Asymptotic homogenization

For completeness, we briefly review the basic theory of asymptotic homogenization and describe the novel implementation. The detailed background can be found in Refs. [34–36,49].

3.1.1. Basic theory

One-dimensional periodic structures consist of an array of identical micro-structures along the longitudinal direction. A micro-structure is defined as a unit-cell. Fig. 4 shows the schematic diagram of a periodic structure and the corresponding unit-cell. For convenience, two sets of coordinate systems are defined, one for the unit-cell and one for the full structure. They are $O-y_1y_2y_3$ and $O-x_1x_2x_3$, respectively. The length of a unit-cell is denoted as l, and the length of the corresponding full structure is denoted as L. These two length parameters satisfy $\frac{l}{L}=\epsilon \ll 1$. The domain of the full structure is defined as $\Omega_\epsilon = \{(x_1,x_2,x_3)| -L/2 \le x_1 \le L/2\}$, and the periodic and non-periodic boundaries are defined by S_u and S_ϵ, respectively. The domain of a unit-cell is defined as $Y^\epsilon = \{(y_1,y_2,y_3)| -l/2 \le y_1 \le l/2\}$. The periodic and non-periodic boundaries of a unit-cell are defined as $\omega_\pm$ and S, respectively.

Asymptotic homogenization theory has been developed based on linear elasticity theory. Under an elastic deformation assumption, the relationship between stress σ_{ij}, strain ϵ_{ij} and displacement u_j of a macroscopic beam satisfies

$$\begin{cases} \frac{\partial \sigma_{ij}}{\partial x_j} - f_i^\epsilon = 0, & in\ \Omega_\epsilon \\ \sigma_{ij} = E_{ijkl}\epsilon_{kl}, & in\ \Omega_\epsilon \\ \epsilon_{ij} = \frac{1}{2}\left(\frac{\partial u_i}{\partial x_j} + \frac{\partial u_j}{\partial x_i}\right), & in\ \Omega_\epsilon \end{cases}, \tag{8}$$

where f_i^ϵ denotes a body force, E_{ijkl} is an elasticity coefficient, and i and j are both from 1 to 3. The three expressions in Eq. (8) describe the force equilibrium condition, the constitutive condition of an elastic material, and the compatibility condition of deformation, respectively. Considering the significant size difference between the macroscopic beam and the microscopic unit-cell, the relationship between macroscopic and microscopic coordinates can be constructed as

$$(y_1, y_2, y_3) = \frac{1}{\epsilon}(x_1, x_2, x_3). \tag{9}$$

According to perturbation expansion theory, any function Φ^ϵ can be expanded as

$$\Phi^\epsilon(x_1,x_2,x_3) = \Phi^0(x_1,y_1,y_2,y_3) + \epsilon\Phi^1(x_1,y_1,y_2,y_3) + \epsilon^2\Phi^2(x_1,y_1,y_2,y_3) + \dots. \tag{10}$$

Then the derivative of function Φ^ϵ with respect to coordinates x_i can be written as

$$\begin{cases} \frac{d\Phi^\epsilon}{dx_1} = \frac{\partial \Phi^\epsilon}{\partial x_1} + \frac{1}{\epsilon}\frac{\partial \phi^\epsilon}{\partial y_1} \\ \frac{d\Phi^\epsilon}{dx_2} = \frac{1}{\epsilon}\frac{\partial \Phi^\epsilon}{\partial y_2} \\ \frac{d\Phi^\epsilon}{dx_3} = \frac{1}{\epsilon}\frac{\partial \Phi^\epsilon}{\partial y_3} \end{cases}. \tag{11}$$

Note that the function Φ^ϵ is not periodic in the x_2 and x_3 directions, and therefore the derivatives with respect to x_2 and x_3 do not have a dual-scale characteristic, which can be obtained directly through the transformation relation between the macroscopic and microscopic coordinates. Similarly, displacement and stress fields can also be expanded as

$$\begin{cases} u_i(\mathbf{x},\mathbf{y}) = u_i^{(0)}(\mathbf{x}) + \epsilon \cdot u_i^{(1)}(\mathbf{x},\mathbf{y}) + \epsilon^2 \cdot u_i^{(2)}(\mathbf{x},\mathbf{y}) + \dots, & i = 1,2,3 \\ \sigma_{ij}(\mathbf{x},\mathbf{y}) = \sigma_{ij}^{(0)}(\mathbf{x}) + \epsilon \cdot \sigma_{ij}^{(1)}(\mathbf{x},\mathbf{y}) + \epsilon^2 \cdot \sigma_{ij}^{(2)}(\mathbf{x},\mathbf{y}) + \dots, & i,j = 1,2,3 \end{cases}. \tag{12}$$

Plugging Eqs. (11) and (12) into the governing equations in elastic mechanics [48], and after some mathematical manipulations, the zeroth-order and first-order displacement fields can be further written as

$$\begin{cases} u_1^{(0)} = 0 \\ u_\alpha^{(0)} = w_\alpha(x_1) \\ u_1^{(1)} = v_1^{(1)}(x_1) - y_\alpha \frac{\partial w_\alpha(x_1)}{\partial x_1} \\ u_\alpha^{(1)} = v_\alpha^{(1)}(x_1) - \epsilon_{\alpha\beta} y_\beta \bar{\Phi}(x_1) \end{cases}, \tag{13}$$

where α and β are both taken from 2 to 3. Here $\epsilon_{\alpha\beta}$ satisfies the rule of $\epsilon_{23} = -1$, $\epsilon_{32} = 1$ and $\epsilon_{22} = \epsilon_{33} = 0$. $\bar{\Phi}$ is the torsional angle around the x_1 axis, and w_α is the bending deflection with respect to axis x_α. $v_1^{(1)}$ and $v_\alpha^{(1)}$ represent the macroscopic displacement of the neutral axis under tension and bending conditions, respectively. These macroscopic parameters are only related to the macroscopic coordinate x_1. The tension strain $\bar{\epsilon}_1$, bending curvature $\bar{\kappa}_\alpha$ and torsional curvature $\bar{\kappa}_1$ can be calculated through

$$\begin{cases} \bar{\epsilon}_1 = \frac{\partial v_1^{(1)}}{\partial x_1} \\ \bar{\kappa}_\alpha = \frac{\partial^2 w_\alpha}{\partial x_\alpha^2} \\ \bar{\kappa}_1 = \frac{\partial \bar{\Phi}}{\partial x_1} \end{cases}. \tag{14}$$

It is assumed that second-order displacement fields can be obtained through a linear superposition of first-order strain fields, which can be expressed as

$$u_m^{(2)} = U_m^{11}(y_1)\bar{\epsilon}_1 + V_m^{\alpha 1}(y_1)\bar{\kappa}_\alpha + W_m^{11}(y_1)\bar{\kappa}_1, \qquad m = 1,\ 2,\ 3. \tag{15}$$

Therefore, the total displacement field to second-order can be expressed as

$$\begin{cases} u_1 = \epsilon(v_1^{(1)}(x_1) - y_\alpha \frac{\partial w_\alpha(x_1)}{\partial x_1}) + \epsilon^2(U_1^{11}(y_1)\bar{\epsilon}_1 + V_1^{\alpha 1}(y_1)\bar{\kappa}_\alpha + W_1^{11}(y_1)\bar{\kappa}_1) + O(\epsilon^3) \\ u_\alpha = w_\alpha(x_1) + \epsilon(v_\alpha^{(1)}(x_1) - \epsilon_{\alpha\beta} y_\beta \bar{\phi}(x_1)) + \epsilon^2(U_\alpha^{11}(y_1)\bar{\epsilon}_1 + V_\alpha^{\beta 1}(y_1)\bar{\kappa}_\beta + W_\alpha^{11}(y_1)\bar{\kappa}_1) + O(\epsilon^3) \end{cases}, \tag{16}$$

where U_m^{11}, $V_m^{\alpha 1}$ and W_m^{11} are the characteristic displacement fields of the microscopic unit-cell structure, which can be obtained by solving the unit-cell equations under tension, bending and torsion. The unit-cell equation under tension can be expressed as

$$\begin{cases} \frac{\partial}{\partial y_j}(E_{ijkl}\frac{\partial U_k^{11}}{\partial y_l} + E_{ij11}) = 0, & \text{in} \quad Y \\ (E_{ijkl}\frac{\partial U_k^{11}}{\partial y_l} + E_{ij11})n_j = 0, & \text{on} \quad S \\ E_{ijkl}\frac{\partial U_k^{11}}{\partial y_l} n_j|_{\omega_+} = -E_{ijkl}\frac{\partial U_k^{11}}{\partial y_l} n_j|_{\omega_-}, & \text{on} \quad \omega_\pm \\ U_k^{11}|_{\omega_+} = U_k^{11}|_{\omega_-}, & \text{on} \quad \omega_\pm \end{cases}. \tag{17}$$

The unit-cell equation under bending can be expressed as

$$\begin{cases} \frac{\partial}{\partial y_j}(E_{ijkl}\frac{\partial V_k^{\alpha 1}}{\partial y_l} - y_\alpha E_{ij11}) = 0, & \text{in} \quad Y \\ (E_{ijkl}\frac{\partial V_k^{\alpha 1}}{\partial y_l} - y_\alpha E_{ij11})n_j = 0, & \text{on} \quad S \\ E_{ijkl}\frac{\partial V_k^{\alpha 1}}{\partial y_l} n_j|_{\omega_+} = -E_{ijkl}\frac{\partial V_k^{\alpha 1}}{\partial y_l} n_j|_{\omega_-}, & \text{on} \quad \omega_\pm \\ V_k^{\alpha 1}|_{\omega_+} = V_k^{\alpha 1}|_{\omega_-}, & \text{on} \quad \omega_\pm \end{cases}. \tag{18}$$

The unit-cell equation under torsion can be expressed as

$$\begin{cases} \frac{\partial}{\partial y_j}(E_{ijkl}\frac{\partial W_k^{11}}{\partial y_l} + \epsilon_{\alpha\beta} y_\beta E_{ij\alpha 1}) = 0, & \text{in} \quad Y^\epsilon \\ (E_{ijkl}\frac{\partial W_k^{11}}{\partial y_l} + \epsilon_{\alpha\beta} y_\beta E_{ij\alpha 1})n_j = 0, & \text{on} \quad S \\ E_{ijkl}\frac{\partial W_k^{11}}{\partial y_l} n_j|_{\omega_+} = -E_{ijkl}\frac{\partial W_k^{11}}{\partial y_l} n_j|_{\omega_-}, & \text{on} \quad \omega_\pm \\ W_k^{11}|_{\omega_+} = W_k^{11}|_{\omega_-}, & \text{on} \quad \omega_\pm \end{cases}. \tag{19}$$

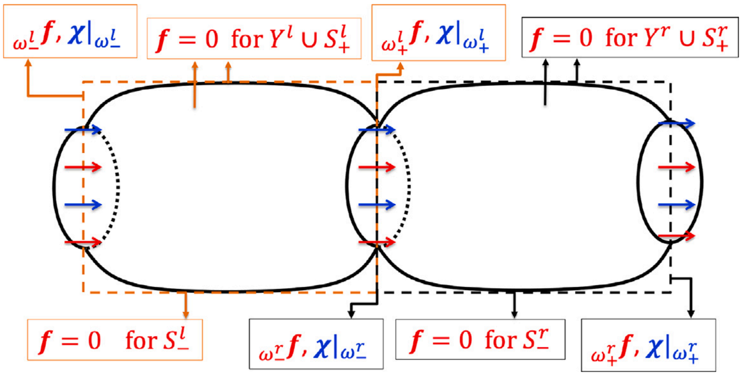

Fig. 5. Force equilibrium and displacement continuity conditions of double unit-cell structures. For periodic boundaries: subscripts ω_-^l, ω_-^r represent left boundary of left and right unit-cells, ω_+^l, ω_+^r right boundary of left and right unit-cells, f, χ force and displacement fields in the unit-cell domain. $_{\omega_+^r}f$, $\chi|_{\omega_+^r}$ denote force and displacement fields on right boundary of right unit-cell, and $_{\omega_-^r}f$, $\chi|_{\omega_-^r}$, $_{\omega_+^l}f$, $\chi|_{\omega_+^l}$, $_{\omega_-^l}f$ and $\chi|_{\omega_-^l}$ have been defined in a similar manner. Y^l, S_+^l, S_-^l and Y^r, S_+^r, S_-^r represent the domain, the top boundary and the bottom boundary of left and right unit-cells.

The first expressions in Eqs. (17), (18), (19) represent the body force equilibrium condition in the unit-cell domain, the second the surface force equilibrium condition on the non-periodic boundaries of the unit-cell, the third the surface force equilibrium condition on the periodic boundaries, and the fourth the displacement continuity condition on the periodic boundaries. Fig. 5 visualizes these force equilibrium and displacement continuity conditions.

Under the periodic boundary conditions, to solve the above unit-cell equations, first-order stress fields can be expressed in the form of displacement fields, i.e.

$$\begin{cases} b_{ij}^1 = E_{ijkl}\dfrac{\partial U_k^{11}}{\partial y_l} + E_{ij11}, & \text{Tension} \\ b_{ij}^\alpha = E_{ijkl}\dfrac{\partial V_k^{\alpha 1}}{\partial y_l} - y_\alpha E_{ij11}, & \text{Bending} \\ b_{ij}^4 = E_{ijkl}\dfrac{\partial W_m^{11}}{\partial y_l} + \epsilon_{\alpha\beta} y_\beta E_{ij\alpha 1}, & \text{Torsion} \end{cases} \tag{20}$$

Therefore, the total stress can be further expressed as

$$\sigma_{ij} = \sigma_{ij}^{(0)} + \epsilon\sigma_{ij}^{(1)} + O(\epsilon^2) = \epsilon(b_{ij}^1\bar{\epsilon}_1 + b_{ij}^\alpha\bar{\kappa}_\alpha + b_{ij}^4\bar{\kappa}_1) + O(\epsilon^2). \tag{21}$$

Ignoring shear and buckling effects, periodic structures are equivalent to Euler–Bernoulli beams, and the corresponding constitutive equation is

$$\begin{Bmatrix} N_1 \\ M_2 \\ M_3 \\ T_1 \end{Bmatrix} = \begin{bmatrix} D_{11} & D_{12} & D_{13} & D_{14} \\ D_{21} & D_{22} & D_{23} & D_{24} \\ D_{31} & D_{32} & D_{33} & D_{34} \\ D_{41} & D_{42} & D_{43} & D_{44} \end{bmatrix} \begin{Bmatrix} \bar{\epsilon}_1 \\ \bar{\kappa}_2 \\ \bar{\kappa}_3 \\ \bar{\kappa}_1 \end{Bmatrix}, \tag{22}$$

where D_{11} is the tension stiffness in the longitudinal direction. D_{22} and D_{33} are the bending stiffness with respect to axis x_2 and x_3, respectively. D_{44} is the torsional stiffness around axis x_1. The off-diagonal elements are the coupling stiffness coefficients. In asymptotic homogenization theory, the resultant forces and moments in the unit-cell domain can be denoted as

$$\begin{cases} N_1 = \langle \sigma_{11}^{(1)} \rangle \\ M_\alpha = \langle -y_\alpha \sigma_{11}^{(1)} \rangle \\ T_1 = \langle \epsilon_{\alpha\beta} y_\beta \sigma_{\alpha 1}^{(1)} \rangle \end{cases}, \tag{23}$$

where the operator $\langle\rangle$ is a homogenization operator, which is defined by Eq. (24). Given any quantity ψ, the homogenization solution of $\langle\psi\rangle$ is

$$\langle\psi\rangle = \frac{1}{|Y|}\int_Y \psi\, dy_1 dy_2 dy_3 = \frac{1}{l}\int_Y \psi\, dy_1 dy_2 dy_3. \tag{24}$$

Plugging Eq. (21) into Eq. (23), and according to the definition of effective stiffness in Eq. (22), we have

$$\begin{Bmatrix} N_1 \\ M_2 \\ M_3 \\ T_1 \end{Bmatrix} = \begin{bmatrix} \langle b_{11}^1 \rangle & \langle b_{11}^2 \rangle & \langle b_{11}^3 \rangle & \langle b_{11}^4 \rangle \\ \langle -y_2 b_{11}^1 \rangle & \langle -y_2 b_{11}^2 \rangle & \langle -y_2 b_{11}^3 \rangle & \langle -y_2 b_{11}^4 \rangle \\ \langle -y_3 b_{11}^1 \rangle & \langle -y_3 b_{11}^2 \rangle & \langle -y_3 b_{11}^3 \rangle & \langle -y_3 b_{11}^4 \rangle \\ \langle \epsilon_{\alpha\beta} y_\beta b_{\alpha 1}^1 \rangle & \langle \epsilon_{\alpha\beta} y_\beta b_{\alpha 1}^2 \rangle & \langle \epsilon_{\alpha\beta} y_\beta b_{\alpha 1}^3 \rangle & \langle \epsilon_{\alpha\beta} y_\beta b_{\alpha 1}^4 \rangle \end{bmatrix} \begin{Bmatrix} \bar{\epsilon}_1 \\ \bar{\kappa}_2 \\ \bar{\kappa}_3 \\ \bar{\kappa}_1 \end{Bmatrix}. \tag{25}$$

Therefore, to solve the effective property of a periodic beam structure, the first step is to calculate the characteristic displacements U_k^{11}, $V_k^{\alpha 1}$ and W_k^{11} which are the solution to the unit-cell Eqs. (17), (18) and (19). Then the stress fields b_{ij}^1, b_{ij}^2, b_{ij}^3 and b_{ij}^4 can be calculated by plugging the characteristic displacements into Eq. (20). Finally, the effective stiffness is obtained from Eq. (25).

3.1.2. Implementation of asymptotic homogenization

In Section 3.1.1, the derivation of asymptotic homogenization has been introduced. In this section, we introduce the finite element implementation of the AH method. We express unit-cell Eqs. (17), (18) and (19) in a generalized form as

$$\begin{cases} \frac{\partial b_{ij}}{\partial y_j} = 0, & \text{in } Y \\ b_{ij} n_j = 0, & \text{on } S \\ b_{ij} n_j |_{\omega_+} = -b_{ij} n_j |_{\omega_-}, & \text{on } \omega_\pm \\ u_i |_{\omega_+} = u_i |_{\omega_-}, & \text{on } \omega_\pm \end{cases}. \tag{26}$$

Based on the virtual work principle, for any virtual displacement v_i, we have

$$\int_Y v_i b_{ij,j} dY - \int_S v_i b_{ij} n_j dS - \int_{\omega_+} v_i b_{ij} n_j dS - \int_{\omega_-} v_i b_{ij} n_j dS = 0. \tag{27}$$

Since the corresponding displacement field must satisfy continuity conditions between neighboring unit-cells, the sum of the third and fourth terms of Eq. (27) must be zero, and only the first two terms are left. Then applying integration by parts and the Gauss theorem on the first term, Eq. (27) can be written as

$$\begin{aligned} & \int_Y v_i b_{ij,j} dY - \int_S v_i b_{ij} n_j dS = \int_Y (v_i b_{ij})_{,j} dY - \int_Y v_{i,j} b_{ij} dY - \int_S v_i b_{ij} n_j dS \\ & = \int_S v_i b_{ij} n_j dS + \int_{\omega_+} v_i b_{ij} n_j dS + \int_{\omega_-} v_i b_{ij} n_j dS - \int_Y v_{i,j} b_{ij} dY - \int_S v_i b_{ij} n_j dS \\ & = - \int_Y v_{i,j} b_{ij} dY. \end{aligned} \tag{28}$$

Plugging Eq. (28) into Eq. (27), we can obtain the weak form of an effective integration, which can be expressed as

$$\int_Y v_{i,j} b_{ij} dY = 0. \tag{29}$$

Plugging Eq. (20) into Eq. (29), then using the finite element method to discretize the displacement fields, based on the principle of minimum potential energy, the finite element form of the unit-cell equation can be written as

$$\begin{cases} \mathbf{K}\chi^1 = \mathbf{f}^1 \\ \mathbf{K}\chi^\alpha = \mathbf{f}^\alpha \\ \mathbf{K}\chi^4 = \mathbf{f}^4 \end{cases}, \tag{30}$$

where

$$\mathbf{K} = \int_Y \mathbf{B}^T \mathbf{E} \mathbf{B} dY \tag{31}$$

and

$$\begin{cases} \mathbf{f}^1 = \int_Y \mathbf{B}^T \mathbf{E} \epsilon_0^1 dY \\ \mathbf{f}^\alpha = \int_Y \mathbf{B}^T \mathbf{E} \epsilon_0^\alpha dY \\ \mathbf{f}^4 = \int_Y \mathbf{B}^T \mathbf{E} \epsilon_0^4 dY \end{cases}. \tag{32}$$

In Eqs. (31) and (32), $\mathbf{K}$ is the total stiffness matrix, $\mathbf{B}$ is the matrix of strain–displacement relationships, and $\mathbf{E}$ is the material constitutive matrix. χ^1, χ^α and χ^4 are the total nodal displacement vectors corresponding to the characteristic displacement fields $-U^{11}$, $-V^{\alpha 1}$ and $-W^{11}$. $\mathbf{f}^1$, $\mathbf{f}^\alpha$ and $\mathbf{f}^4$ are the nodal force vectors due to unit strain fields which can be defined as

$$\epsilon = \begin{Bmatrix} \epsilon_{11} \\ \epsilon_{22} \\ \epsilon_{33} \\ \gamma_{xy} \\ \gamma_{yz} \\ \gamma_{zx} \end{Bmatrix}, \quad \epsilon_0^1 = \begin{Bmatrix} 1 \\ 0 \\ 0 \\ 0 \\ 0 \\ 0 \end{Bmatrix}, \quad \epsilon_0^\alpha = \begin{Bmatrix} -y_\alpha \\ 0 \\ 0 \\ 0 \\ 0 \\ 0 \end{Bmatrix}, \quad \epsilon_0^4 = \begin{Bmatrix} 0 \\ 0 \\ 0 \\ -y_3 \\ 0 \\ y_2 \end{Bmatrix}, \tag{33}$$

where ϵ_0^1, ϵ_0^α and ϵ_0^4 represent the strain in tension, bending and torsion, respectively. After the characteristic displacement fields are obtained, the characteristic stress fields can be expressed in finite element form, i.e.

$$\begin{cases} \mathbf{b}^1 = \mathbf{E}(\epsilon_0^1 - \epsilon^1) \\ \mathbf{b}^\alpha = \mathbf{E}(\epsilon_0^\alpha - \epsilon^\alpha) \\ \mathbf{b}^4 = \mathbf{E}(\epsilon_0^4 - \epsilon^4) \end{cases}, \tag{34}$$

where $\epsilon^1 = \mathbf{B}\chi^1$, $\epsilon^\alpha = \mathbf{B}\chi^\alpha$, and $\epsilon^4 = \mathbf{B}\chi^4$ are the characteristic strain fields due to the characteristic displacement fields. Therefore, the effective stiffness matrix can be expressed in the form of strain energy, i.e.

$$D_{ij}^H = \frac{1}{Y}\int_Y (\epsilon_0^i - \epsilon^i)\mathbf{E}(\epsilon_0^j - \epsilon^j)dY, \qquad i,j = 1,\dots,4. \tag{35}$$

3.1.3. Novel implementation of asymptotic homogenization

Although Section 3.1.2 gives the finite element implementation of asymptotic homogenization, it is still difficult to use commercial software to execute calculations. This is not only due to the difficulty of applying the corresponding unit strain fields in FEM software, but also because the FEM implementation of the strain–displacement relationship depends on the element type. Each unit-cell finite element model requires a lot of coding work and tedious mathematical derivation to produce the AH calculation, which must be repeated for a new choice of finite element model. In 2013, Cheng et al. [49] proposed a novel implementation of asymptotic homogenization which is known as NIAH. In NIAH, the effective stiffness matrix is expressed in terms of displacement fields rather than strain fields, and finite element software is used as a black box to execute FEM calculations, which greatly improves the computational efficiency. In NIAH, the force fields are expressed in terms of displacement fields, and accordingly the force in Eq. (32) can be expressed as

$$\begin{cases} \mathbf{f}^1 = \int_Y \mathbf{B}^T\mathbf{E}\epsilon_0^1 dY = \mathbf{K}\chi_0^1 \\ \mathbf{f}^\alpha = \int_Y \mathbf{B}^T\mathbf{E}\epsilon_0^\alpha dY = \mathbf{K}\chi_0^\alpha \\ \mathbf{f}^4 = \int_Y \mathbf{B}^T\mathbf{E}\epsilon_0^4 dY = \mathbf{K}\chi_0^4 \end{cases}. \tag{36}$$

In NIAH, applying the corresponding displacement fields χ_0^i on all nodes, and after a static calculation, nodal force fields $\mathbf{f}^i$ can be obtained with ease. For solid finite elements, every node has three translational degrees of freedom, and the displacement field under unit strain conditions can be expressed as

$$\chi_0^i = \begin{Bmatrix} u \\ v \\ w \end{Bmatrix}, \quad \chi_0^1 = \begin{Bmatrix} y_1 \\ 0 \\ 0 \end{Bmatrix}, \quad \chi_0^2 = \begin{Bmatrix} -y_1y_2 \\ y_1^2/2 \\ 0 \end{Bmatrix}, \quad \chi_0^3 = \begin{Bmatrix} -y_1y_3 \\ 0 \\ y_1^2/2 \end{Bmatrix}, \quad \chi_0^4 = \begin{Bmatrix} 0 \\ -y_1y_3 \\ y_1y_2 \end{Bmatrix}. \tag{37}$$

For beam or shell finite elements, three rotational degrees of freedom must also be included, and the corresponding displacement fields are

$$\chi_0^i = \begin{Bmatrix} u \\ v \\ w \\ \theta_{y_1} \\ \theta_{y_2} \\ \theta_{y_3} \end{Bmatrix}, \quad \chi_0^1 = \begin{Bmatrix} y_1 \\ 0 \\ 0 \\ 0 \\ 0 \\ 0 \end{Bmatrix}, \quad \chi_0^2 = \begin{Bmatrix} -y_1y_2 \\ y_1^2/2 \\ 0 \\ 0 \\ 0 \\ y_1 \end{Bmatrix}, \quad \chi_0^3 = \begin{Bmatrix} -y_1y_3 \\ 0 \\ y_1^2/2 \\ 0 \\ -y_1 \\ 0 \end{Bmatrix}, \quad \chi_0^4 = \begin{Bmatrix} 0 \\ -y_1y_3 \\ y_1y_2 \\ y_1 \\ 0 \\ 0 \end{Bmatrix}, \tag{38}$$

where θ_{y_1}, θ_{y_2} and θ_{y_3} represent three rotational degrees of freedom. After obtaining the force field, Eq. (32), the unit-cell equation (30) can be solved with periodic boundary conditions. To describe the unit-cell equation (30) better, a transformation matrix $\mathbf{T}$ is introduced, which transforms the master nodal degree of freedom $\tilde{\chi}^i$ into the total nodal degree of freedom χ^i by

$$\mathbf{T}\tilde{\chi}^i = \chi^i. \tag{39}$$

Note that for beam or shell finite elements a master node is a node that has six degrees of freedom, which means that it can move in three translational and three rotational degrees of freedom. The finite element form of the unit-cell equation (30) can be written as

$$\tilde{\mathbf{K}}\tilde{\chi}^i = \tilde{\mathbf{f}}^i, \tag{40}$$

where $\tilde{\mathbf{K}} = \mathbf{T}^T\mathbf{K}\mathbf{T}$ and $\tilde{\mathbf{f}}^i = \mathbf{T}^T\mathbf{f}^i$.

In NIAH calculations using commercial FEM software, the periodic boundary conditions can be implemented by coupling the nodal degrees of freedom of two periodic boundaries of the unit-cell. Applying the nodal force $\mathbf{f}^i$ and the periodic boundary conditions on the unit-cell, after a static FEM calculation, the characteristic displacement field χ^i can be obtained. Note that to avoid a singularity of the total stiffness matrix, rigid-body motions should be excluded in the FEM implementation by constraining

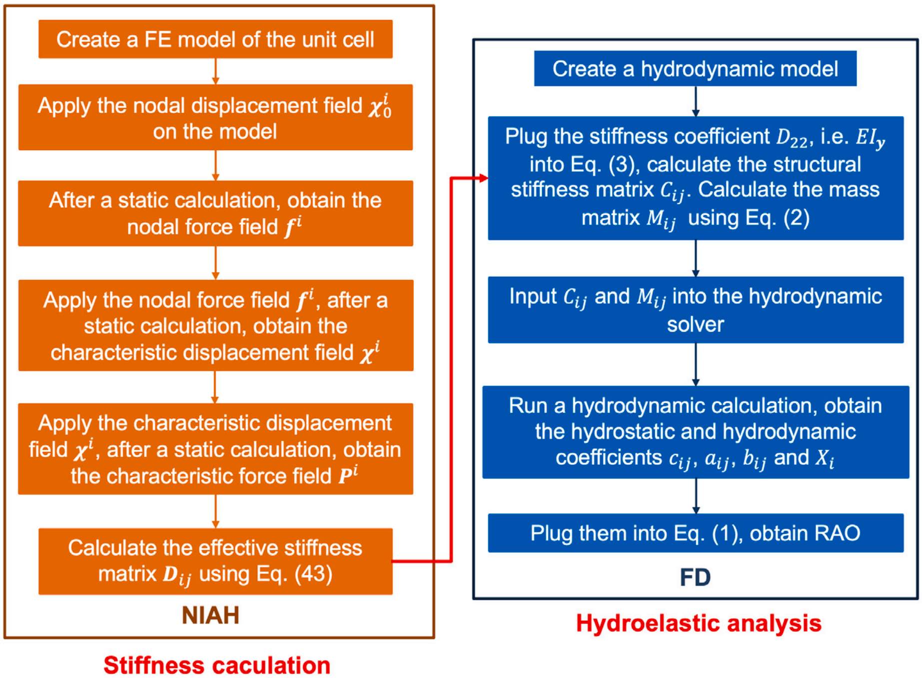

Fig. 6. A new workflow of the efficient analysis of hydroelastic solution.

the degrees of freedom of any master node. Then the stiffness matrix Eq. (35) can be expressed in terms of initial displacement fields χ_0^i and characteristic displacement fields χ^i, i.e.

$$D_{ij} = \frac{1}{|Y|}(\chi_0^i - \chi^i)^T \mathbf{K}(\chi_0^j - \chi^j), \quad i, j = 1, \dots, 4. \tag{41}$$

To avoid assembling the total stiffness matrix $\mathbf{K}$, applying the characteristic displacement field χ^i on the unit-cell, then running a static FEM calculation, the nodal reaction force $\mathbf{P}^i$ can be obtained, which can also be solved analytically by

$$\mathbf{P}^i = \mathbf{K}\chi^i. \tag{42}$$

Finally, the equivalent stiffness matrix can be written as

$$D_{ij} = \frac{1}{|Y|}(\chi_0^i - \chi^i)^T (\mathbf{f}^j - \mathbf{P}^j). \tag{43}$$

In NIAH calculations, commercial FEM software can directly output the parameters on the right-hand side of Eq. (43), and then the effective stiffness can be calculated easily.

3.2. Efficient analysis workflow for the hydroelastic problem

In this paper, we use the NIAH method to calculate the structural stiffness of periodic floating structures, and develop an efficient analysis workflow for solving the hydroelastic problem. Fig. 6 illustrates this new workflow. Similar to the workflow shown in Fig. 3, this new workflow also includes two modules, i.e. the structural stiffness calculation and the hydroelastic analysis. To solve the structural stiffness, we take commercial FEM software as a black box to execute the NIAH calculation. The first step is to create a unit-cell model of the periodic structure. Then applying the initial nodal displacement field χ_0^i on the unit-cell, running a static calculation, the nodal force field $\mathbf{f}^i$ can be obtained. The next step is to apply the force field $\mathbf{f}^i$ on the unit-cell, and after a static calculation, the characteristic displacement field χ^i can be obtained. Then applying the characteristic displacement field χ^i on the unit-cell, running a static calculation, the characteristic force field $\mathbf{P}^i$ can be obtained. Plugging these parameters into Eq. (43), the effective stiffness coefficients D_{ij} can be computed.

For the hydrodynamic solution, we apply the OceanWave3D-Seakeeping solver [27–29]. Plugging the bending stiffness into Eq. (3), the structural stiffness coefficients C_{ij} can be obtained. Note that in this workflow the vertical bending stiffness EI_y in Eq. (3) is the stiffness coefficient D_{22} which is solved by NIAH. The mass matrix coefficient M_{ij} can be obtained based on Eq. (2). The hydrodynamic coefficients a_{ij}, b_{ij} and X_i are computed from the radiation and diffraction solutions, and the hydrostatic coefficients c_{ij} are computed by numerical integration over the wetted surface. Finally, the motion response can be predicted by plugging all of the coefficients into the equation of motion Eq. (1). The hydrodynamic solutions allow us to study the effects of transverse and

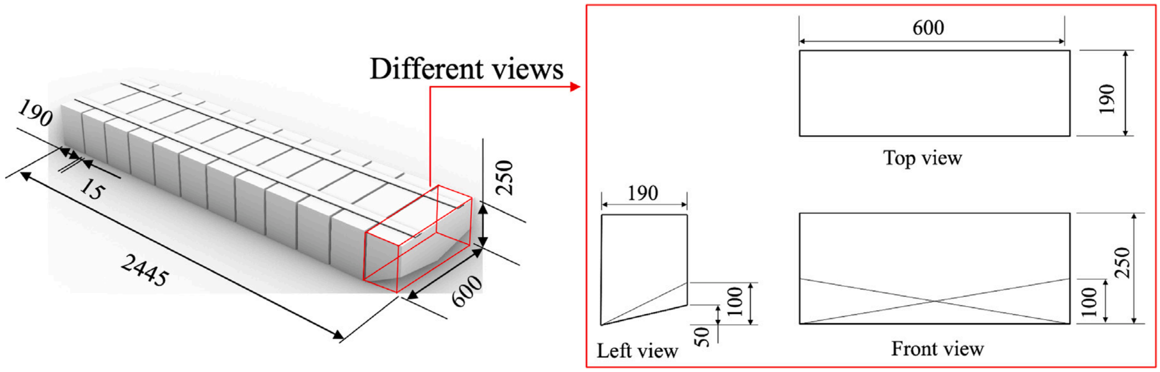

Fig. 7. Birds-eye view of the barge and various views of the bow pontoon for the 6 mm bar case.

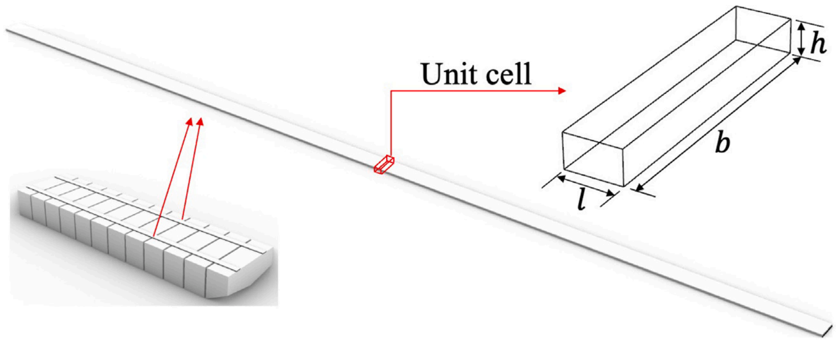

Fig. 8. Unit-cell model in NIAH calculation.

longitudinal stiffeners on the final hydroelastic response of a ship. For more details on the hydrodynamic solution, the reader is referred to Refs. [24–26,28].

4. Validation cases

In this section, the implementation of the new scheme shown in Fig. 6 is validated using several test cases with both solid and thin-walled structures.

4.1. A solid structure

The first validation case is a barge model which was tested experimentally by Malenica et al. [56]. This model consists of 12 pontoons which are connected by two solid rectangular steel bars running the full length of the structure. The bars are 50 mm wide and span a range of thicknesses in order to modify the stiffness. We consider here the two cases of 6 and 4 mm thickness. The barge is 2445 mm × 600 mm × 250 mm. The gap between neighboring pontoons is 15 mm. For the case of the 6 mm bars, the geometry of the bow pontoon is different from the other pontoons, as shown in Fig. 7. In this hydroelastic analysis, a small deformation is assumed so that the neighboring pontoons do not touch each other. Therefore, we assume the structural stiffness is provided only by the steel bars, as shown in Fig. 8. For the steel material, the modulus of elasticity and Poisson's ratio are 210 Gpa and 0.3, respectively.

We use the commercial finite element software ANSYS [32] to apply NIAH and estimate the structural stiffness. The schematic diagram of the unit-cell is shown in Fig. 8. The length of the unit-cell model is denoted as l, the breadth b, the height h. The unit-cell model of $l = 10$ mm, $b = 50$ mm and $h = 6$ mm is used for the stiffness calculation of the 50 mm × 6 mm steel bar, and the unit-cell of $l = 10$ mm, $b = 50$ mm and $h = 4$ mm is used for the 50 mm × 4 mm steel bar. Fig. 9 shows the FEM model of these two unit-cells which are discretized by 3000 and 1360 SOLID95 [32] elements respectively. For convenience we denote the 50 mm × 4 mm model as Model 1 and the 50 mm × 6 mm model as Model 2. Table 1 lists the diagonal coefficients of the structural stiffness matrix and compares the analytical results with the NIAH calculations. The coefficients correspond to: the axial tension stiffness, the vertical and transverse bending stiffness and the torsional stiffness around the axis, respectively. For a rectangular solid section these coefficients are given exactly by

$$D_{11} = Ebh, \quad D_{22} = \frac{Ebh^3}{12}, \quad D_{33} = \frac{Ehb^3}{12}, \quad D_{44} = G\beta bh^3, \tag{44}$$

Table 1
Structural stiffness of solid rectangular beams.

	Method	D_{11} (GN)	D_{22} (GN m^2)	D_{33} (GN m^2)	D_{44} (GN m^2)
Model 1	Analytical	42	56	8750	80.6 – 86.1
	NIAH	42	56	8750	81.8
Model 2	Analytical	63	189	13 125	267.8 – 272.2
	NIAH	63	189	13 125	268.8

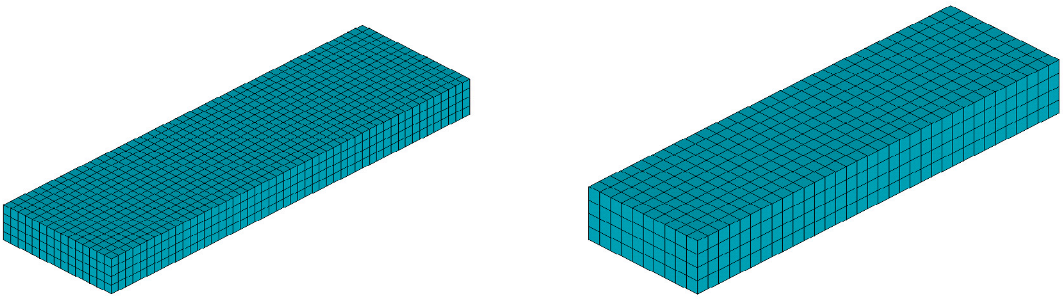

(a) Model 1. (b) Model 2.

Fig. 9. Finite element model of unit-cells.

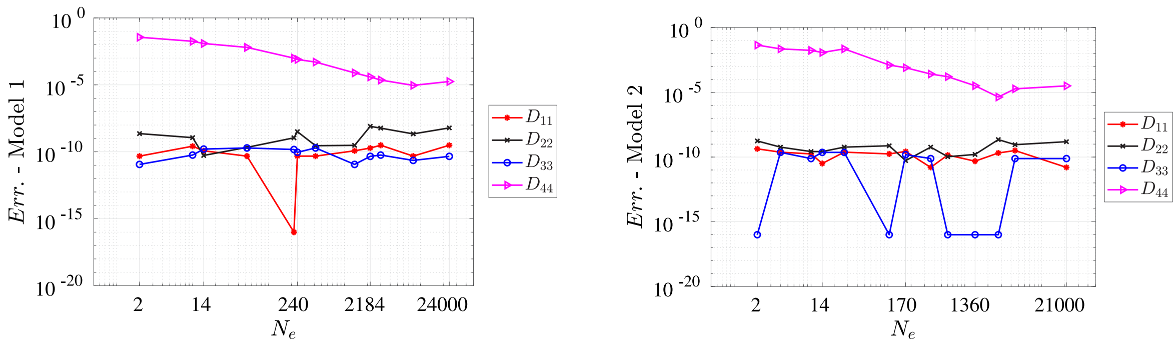

(a) Model 1. (b) Model 2.

Fig. 10. Relative error of structural stiffness by NIAH with increasing number of elements.

where E is the elasticity modulus, and G is the shear modulus which can be obtained from $G = E/2(1+\mu)$ for isotropic materials, where μ is Poisson's ratio. According to [57], $\beta \approx 0.307$ when $b/h = 8$, $\beta \approx 0.312$ when $b/h = 10$, $\beta \approx 0.333$ when $b/h = \infty$. Taking the analytical results as a reference, we carry out a convergence analysis of the structural stiffness with increasing number of elements. The relative error is computed from

$$Err. = \left| \frac{D_{ij}^{NIAH} - D_{ij}^{Ref.}}{D_{ij}^{Ref.}} \right| + \epsilon, \tag{45}$$

where D_{ij}^{NIAH} denotes the structural stiffness calculated by NIAH, and $D_{ij}^{Ref.}$ is the exact value. The value of $\epsilon = 10^{-16}$ is added here for plotting convenience to handle cases of exactly zero error. For the torsional stiffness, the reference values are taken as 81.8 GN m^2 and 268.8 GN m^2 respectively. Fig. 10 shows the relative error in the structural stiffness by NIAH. The horizontal axis N_e represents the number of elements. From Fig. 10, the results can always be seen to agree well with the reference solutions for the tension and bending stiffness. This is because the FEM grids for a solid rectangle are very simple and regular, which allows them to (almost) exactly describe the structural information even for a small number of elements. The torsion stiffness gradually tends to the referenced values with increasing number of elements. Since the torsional references are not exact solutions, the relative error does not tend to machine precision, and the error partially comes from the error associated with the reference values.

In the hydrodynamic calculations, the draft of the wet model is 120 mm, and the gravitational acceleration is taken as 9.81 m/s^2. With respect to the motion modes, heave, pitch and the first four vertical bending modes have been considered in this case. The

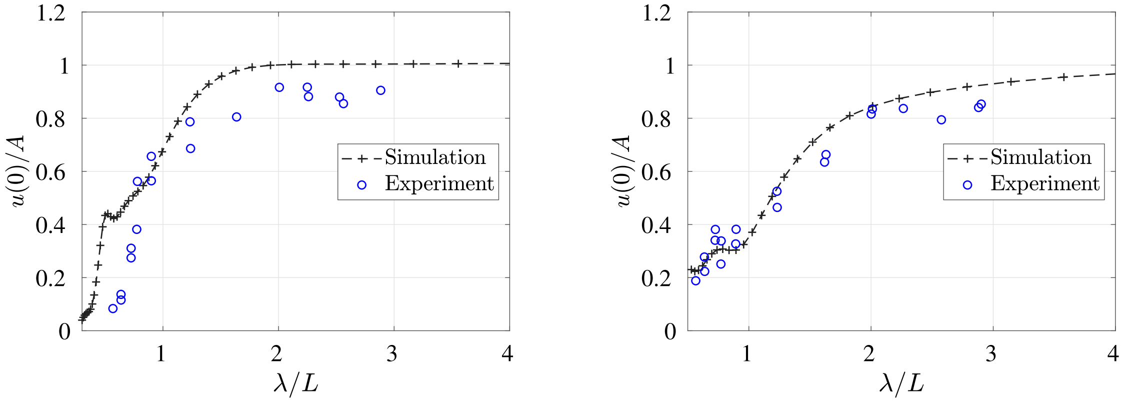

(a) $h = 4$ mm. (b) $h = 6$ mm.

Fig. 11. Vertical displacement response at the mid-ship section.

Table 2
The bending stiffness coefficients of thin-walled box-like structures.

	Method	D_{11} (GN)	D_{22} (GN m^2)	D_{33} (GN m^2)	D_{44} (GN m^2)
Model 1	Dizy [58]	10.3	1.91	5.58	1.71
	Analytical [58]	10.3	1.91	5.58	1.71
	FEM	10.4	1.92	5.58	1.71
	NIAH	10.3	1.91	5.58	1.71
Model 2	Dizy [58]	10.5	1.94	5.62	1.72
	FEM	10.6	1.94	5.66	1.74
	NIAH	10.5	1.94	5.65	1.72
Model 3	Analytical	13.7	2.16	5.58	–
	FEM	13.7	2.17	5.58	1.72
	NIAH	13.7	2.16	5.58	1.72

total vertical displacement response along the ship length is calculated from

$$u(x) = \left| \sum_{j=1}^{6+N} \xi_j h_j^z(x) \right|, \tag{46}$$

where N is the number of flexible modes. The dimensionless result appears in Fig. 11 where A is the incident wave amplitude, λ the wave length and L the ship length. Comparing our numerical solutions with the experimental results from Malenica [56], a general agreement can be seen, though there are some differences especially for the 4 mm bar case. Unfortunately, no error bounds are available for these experiments, so the accuracy is unknown. There are also possible modeling errors associated with our results where the ship hull is approximated by a uniform Euler beam, and shear effects and the torsional deformation are not included. Our geometric model is also continuous, as opposed to the physical model which was composed of 12 discrete pontoons. Also, the structural stiffness in our numerical model is assumed to be provided only by the steel bars while in the physical model, the bar is rigidly attached to each section which may slightly modify the effective overall stiffness.

4.2. Thin-walled structures

In this section, we consider three thin-walled box-like structures. The first one has no reinforced stiffeners, the second one has transverse reinforced stiffeners, and the third one has a longitudinal stiffener. For convenience, they are denoted as Model 1, 2 and 3 respectively, where Models 1 and 2 are taken from Dizy et al. [58]. In Model 2, the distance between neighboring stiffeners is 1 m, and the stiffener thickness is $t = 0.025$ m. In Model 3, the stiffener thickness is $d = 0.05$ m. The global size of the three macroscopic structures is the same, with length $L = 16$ m, breadth $B = 2$ m, height $H = 1$ m, and the wall thickness is $t = 0.025$ m. A schematic diagram of the macroscopic structures and the corresponding microscopic unit-cells is shown in Fig. 12. Fig. 13 shows the FEM models of the unit-cell in the NIAH calculation, and these three unit-cell FEM models are discretized by 2400, 6938 and 3200 SOLID95 [32] elements respectively. Consistent with Dizy et al. [58], the modulus of elasticity and Poisson's ratio are set to 70 Gpa and 0.3, respectively. FEM calculations based on full models are also carried out. Table 2 compares the results showing that the NIAH calculations agree well with the other methods.

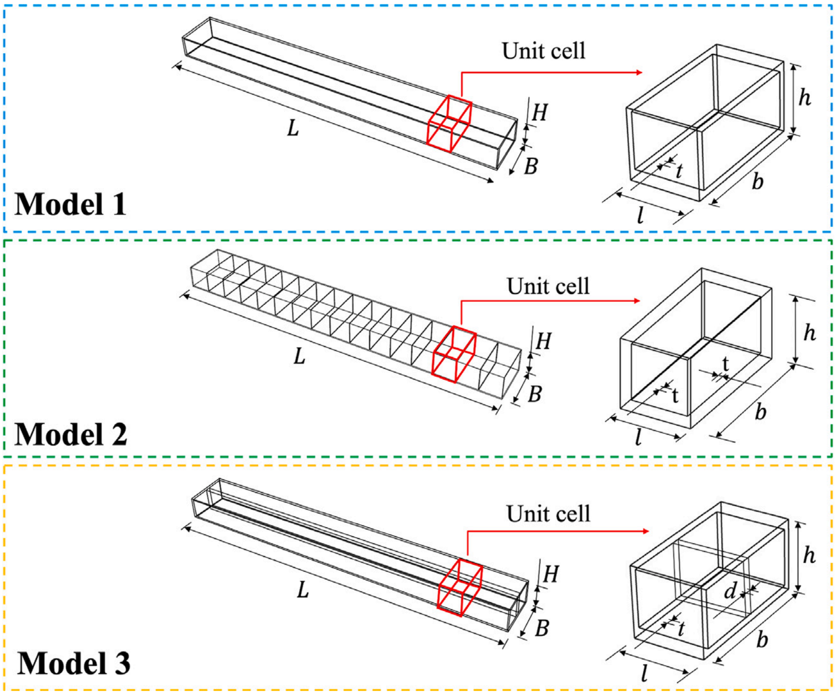

Fig. 12. Three types of thin-walled box-like structures and the corresponding unit-cell models.

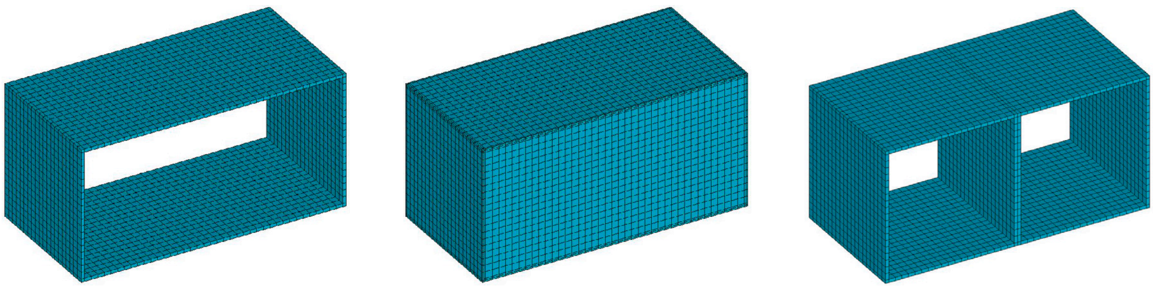

(a) Model 1. (b) Model 2. (c) Model 3.

Fig. 13. The unit-cell FEM model of thin-walled box-like structures.

To analyze the convergence of the stiffness calculations with increasing number of elements, we calculate the relative difference from

$$Diff = \left| \frac{D_{ij}^{NIAH} - D_{ij}^{Ref}}{D_{ij}^{Ref}} \right| + \epsilon, \tag{47}$$

where the reference solution is the analytic value for Model 1, and for the tension and bending stiffness of Model 3. For Model 2 and the torsion stiffness of Model 3, however, there are no exact solutions so we instead take a very fine NIAH model as the reference value. Convergence of the NIAH calculations is shown in Fig. 14. It can be seen that the coefficients generally agree well with the reference values with only small differences associated with increasing number of elements. The calculation errors here come from various sources including geometric imperfections in the FEM model and the grid generation method adopted. For example, for Models 1 and 3, the volume grids are directly extruded from the surface grids, but Model 2 is partitioned into several divisions before meshing. Even so, the calculation accuracy shown here is much higher than typical engineering requirements.

To explore the influence of the reinforced stiffeners on the motion response, we further carry out hydroelastic calculations using OceanWave3D-Seakeeping. Note that in the hydrodynamic analysis, the wet model of these three thin-walled box-like structures is the same with draft 1 m, breadth 2 m, and length 16 m. In this case, surge, heave, pitch and eight vertical bending modes have been considered. Based on Eq. (46), we obtain the frequency-domain solution of the vertical displacement of these three models

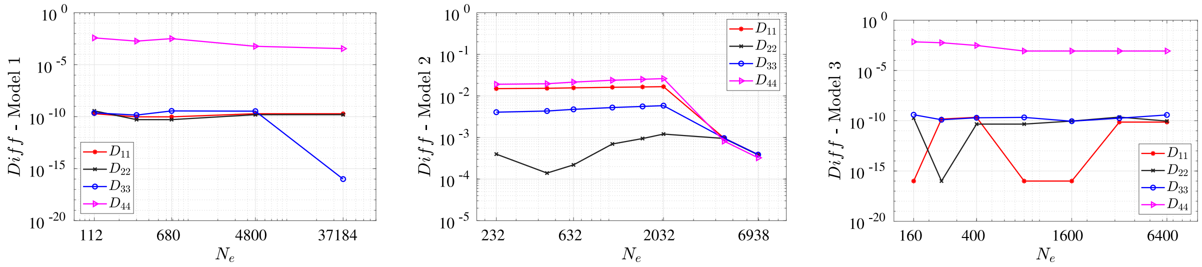

(a) Model 1. (b) Model 2. (c) Model 3.

Fig. 14. Relative error of the structural stiffness by NIAH with increasing number of elements.

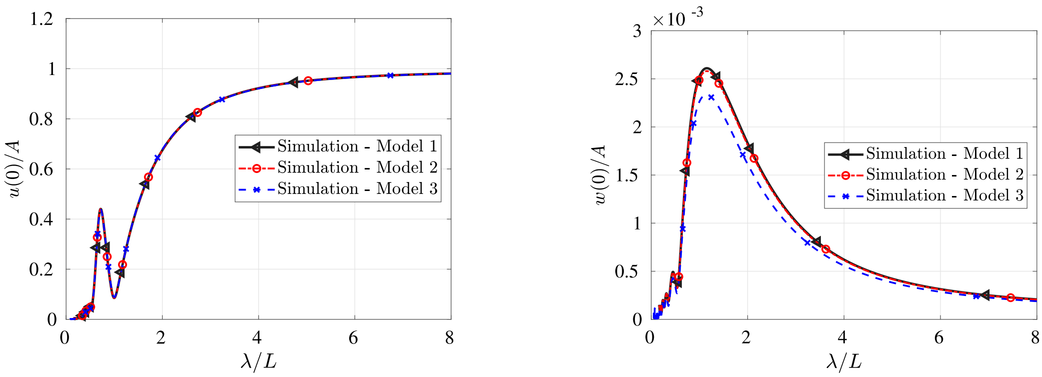

(a) Vertical displacement. (b) Vertical deformation.

Fig. 15. Vertical motion response at the midsection of box-like structures.

at any position, and Fig. 15(a) shows the dimensionless displacement at the mid-ship section. It can be seen that the influence of the stiffeners on the vertical displacement response is small in this case. In addition to the displacement, the structural deformation is also a key parameter in the loading analysis and the structural design of a ship. Ignoring the contributions from the rigid-body modes, the vertical deformation of the structure can be obtained by summing up the motion displacement in all elastic modes using

$$w(x) = \left| \sum_{j=7}^{N} \xi_j h_j^z(x) \right|. \tag{48}$$

Dimensionless results are presented in Fig. 15(b). It is clear that the vertical deformation of Model 3 is generally smaller than Models 1 and 2, showing that the longitudinal stiffeners are effective at reducing the vertical bending deformation. The vertical deformation of Models 1 and 2 are nearly the same, indicating that the transverse stiffeners have little influence on bending, as might be expected since they are mainly used to stiffen the ship in torsion. Although we have not yet implemented torsional modes in our solver, this is planned as future work.

5. Hydroelastic analysis of a container ship

In this section, we apply the new strategy to several representative container ship sections. Fig. 16 illustrates the development of the cross-section model, the unit-cell model, and the full model based on a real container ship. The length of the ship is $L = 400$ m, the breadth $B = 50$ m, and the height $H = 25$ m. The length of the unit-cell is denoted as l, the breadth b, the height h.

Fig. 17 gives a detailed description of the unit-cell model. Considering the structural characteristics of a real ship section, the wall of the model is not approximated by a solid plane, but consists of many hollow cubes with length $a = 2.5$ m and wall thickness $t = 0.125$ m, and in fact the hollow cubes work as the longitudinal and transverse stiffeners. In Fig. 17, sections S1 and S2 show two transverse cuts through the unit-cell while S3, S4 and S5 show three longitudinal cuts. The modulus of elasticity is E = 210 Gpa, and Poisson's ratio $\mu =$ 0.3.

5.1. Convergence with unit-cell size

To instill confidence in the calculations, we perform a convergence analysis with respect to unit-cell size. Three different unit-cell sizes are considered, consisting of 1, 2 and 3 unit-cells, respectively. The unit-cells have been discretized by 25552, 51104

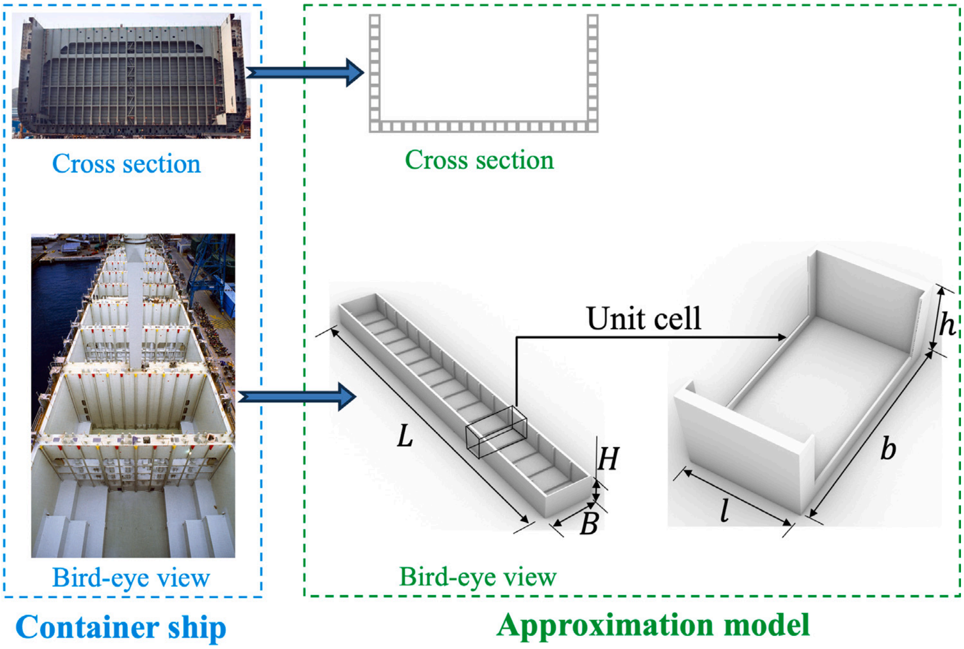

Fig. 16. A container ship and the corresponding unit-cell model.

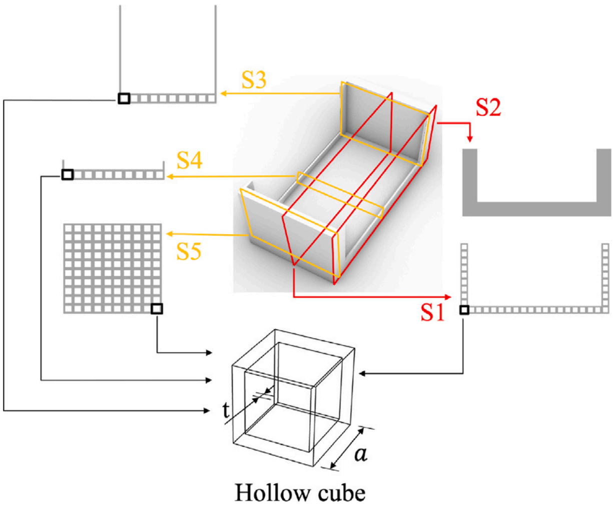

Fig. 17. Schematic diagram of a unit-cell model for a container ship.

and 76656 SOLID95 [32] elements respectively, and the corresponding FEM models are shown in Fig. 18(a) where the transverse cutting plane S1 and the longitudinal cutting plane S4 are shown as well. Using Eq. (47), we calculate the relative difference in the structural stiffness between the three unit-cell models as shown in Fig. 18(b), in which the reference model is the model with 3 unit-cells. Clearly there are only very small differences between these models, which means the model with 1 unit-cell can estimate the coefficients with high precision.

5.2. Influence of stiffeners on the structural stiffness

In practice, the layout of the stiffeners in a ship hull is chosen in order to satisfy all relevant structural requirements. In this section, we study the influence of different numbers of both transverse and longitudinal stiffeners on the global structural stiffness coefficients of a container ship hull. Based on the results from Section 5.1, a 1-unit-cell model (as shown in Fig. 18(a)) is sufficient to produce accurate results, so all calculations are made using a 1-unit-cell. Six structural layouts are chosen, as shown in Fig. 19.

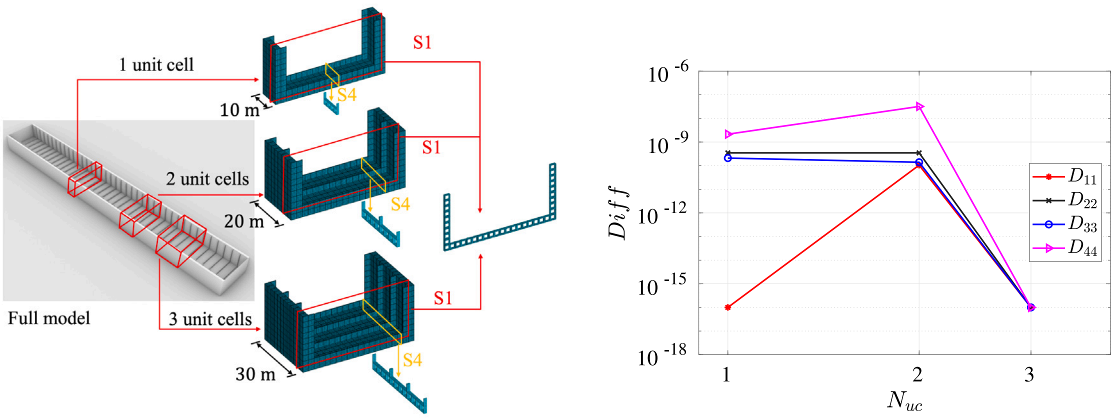

(a) FEM model of various size unit-cells.

(b) Relative stiffness difference between various unit-cells.

Fig. 18. Convergence of the structural stiffness with the increasing unit-cell size.

Table 3
The structural stiffness of the container ship models with different stiffener layouts calculated by NIAH.

	D_{11} (× 10^4 GN)	D_{22} (× 10^6 GN m^2)	D_{33} (× 10^6 GN m^2)	D_{44} (× 10^4 GN m^2)
Model 1	1.904	1.154	7.176	2.190
Model 2	1.899	1.154	7.160	2.172
Model 3	1.897	1.154	7.154	2.166
Model 4	1.984	1.260	7.538	2.202
Model 5	2.005	1.260	7.537	2.185
Model 6	2.055	1.265	7.595	2.185

Model pairs (1, 4), (2, 5), and (3, 6) have transverse stiffener spacings of 10, 20 and 30 m respectively, and this is also the size of the corresponding unit-cell. Model 1 here is exactly the same as the 1-unit-cell model in Section 5.1, as shown in Fig. 19(a). Models 4 to 6 include additional longitudinal stiffeners, as can be seen from the sectional cuts S1. Models 1 to 3 are discretized by 25552, 48656 and 71760 SOLID95 [32] elements respectively, while Models 4 to 6 are discretized by 26344, 50864, 76800 SOLID95 elements respectively

Table 3 lists the structural stiffness results of the six models by NIAH calculations. Comparing the stiffness coefficients between Model pairs (1, 4), (2, 5) and (3, 6), it can be observed that the influence of the longitudinal stiffeners on the tension and bending stiffness is more significant than for the torsional stiffness. Comparing the stiffness between Models 1 to 3, it is clear that the influence of the transverse stiffeners on the tension stiffness and the bending stiffness is very small. These calculations illustrate how the transverse and longitudinal stiffeners influence the global stiffness of a ship hull.

5.3. Motion response

To study the influence of the stiffeners on the final hydroelastic response, we use the strategy of Fig. 6 to calculate the vertical motion response of the six container ship models discussed above. The ship is in head seas, with the waves incident from $\beta = 180°$, where β is the wave propagation direction measured from the positive x-axis. For convenience, in this section, the model draft is assumed to be identical with the structural height, i.e. 25 m. Based on Eq. (46), the total vertical displacement response along the ship length can be calculated. The corresponding dimensionless frequency-domain results at the mid-ship section are shown in Fig. 20. From Fig. 20(a) it is clear that the vertical displacements of Models 1–3 are nearly identical, while from Figs. 20(b), 20(c), 20(d) small reductions can be seen from the longitudinal stiffeners in the shorter-wave range. This illustrates how longitudinal stiffeners are more effective at reducing the vertical bending deformation than transverse stiffeners. The vertical deformation along the ship length due only to the elastic modes is calculated using Eq. (48) and shown in Fig. 21. This figure plots the dimensionless vertical deformation results at nine different positions along the ship in waves of dimensionless wavelength of $\lambda/L = 0.714864$, and the horizontal axis is the ratio of the x coordinate to half the ship length. It can be seen that a relatively large deformation appears at the ship ends, which is consistent with engineering experience.

5.4. Discussion

The proposed workflow can greatly improve the efficiency of a hydroelastic analysis of large floating structures by introducing the asymptotic homogenization method to efficiently estimate the structural stiffness. In Sections 5.1 and 5.2, the length of the

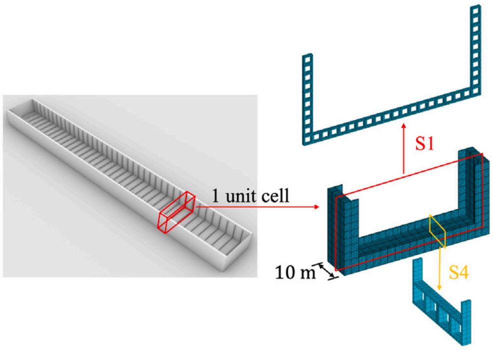

(a) Model 1.

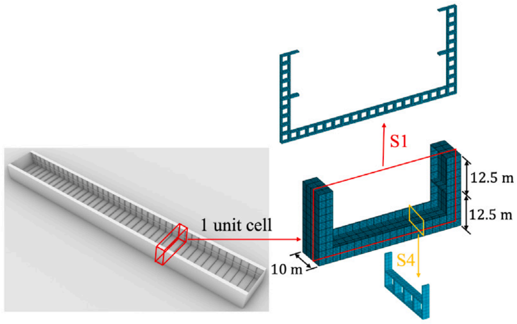

(d) Model 4.

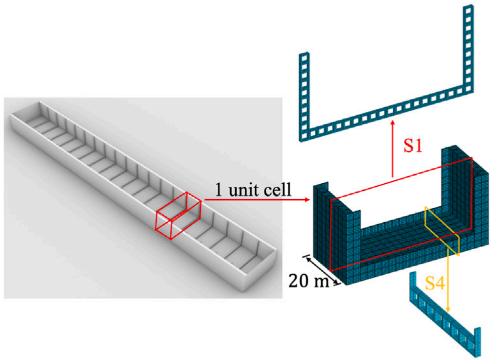

(b) Model 2.

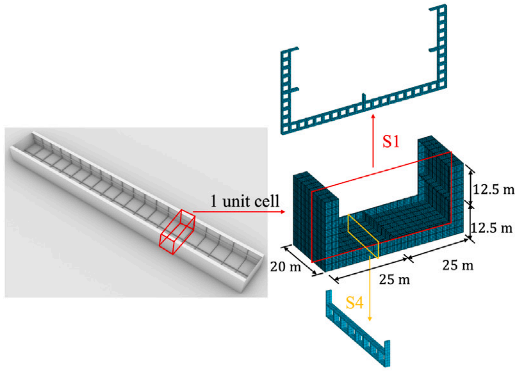

(e) Model 5.

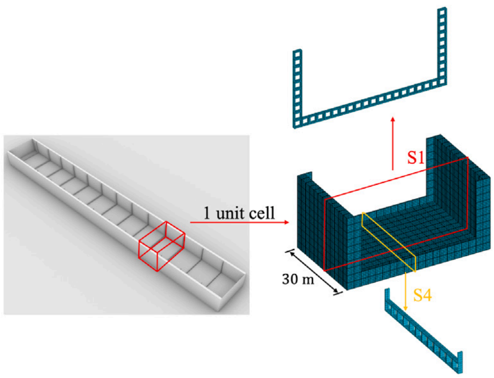

(c) Model 3.

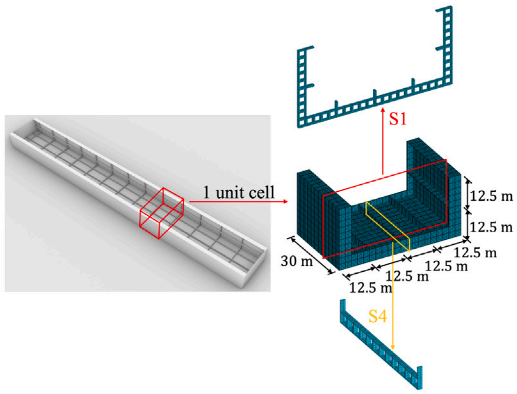

(f) Model 6.

Fig. 19. Finite element models of unit-cells with different transverse and longitudinal stiffener layouts.

unit-cell models (10 m, 20 m, 30 m) and the corresponding full models (400 m) differ by at least an order of magnitude. Using the same FEM discretization strategy for all models, the full model requires respectively 40, 20, and 13.3 times as many degrees of freedom as the corresponding unit-cell models. Similarly, in the first validation case of Section 4.1, the length of the unit-cell and the full solid models are 10 mm and 2445 mm respectively, and in the second validation case of Section 4.2, the length of the unit-cell and the full models are 1 m and 16 m, respectively. Since the computational cost of an FEM analysis scales at least linearly with the number of elements (and usually super-linearly), the cost is at least an order of magnitude larger than that of a unit-cell model. This shows that using the new workflow in Fig. 6 to study the hydroelastic problem for nearly-periodic floating structures is much more efficient than the old workflow based on a full FEM model in Fig. 3.

Large modern ships, which are the target for this analysis, generally have a relatively long parallel mid-body which is very-nearly periodic, but the bow and stern regions are of course rather different. However, the variation of sectional properties in these regions is typically nearly linear, which allows us to propose a very simple strategy for including the end effects into the analysis. To illustrate, consider the 11,400 TEU container ship from the paper by Senjanović et al. [59]. This ship is 363.44 m long, 45.6 m wide and 29.74 m deep, and its vertical and transverse sectional area moments of inertia are plotted in Fig. 22. Here, 'Senjanovic

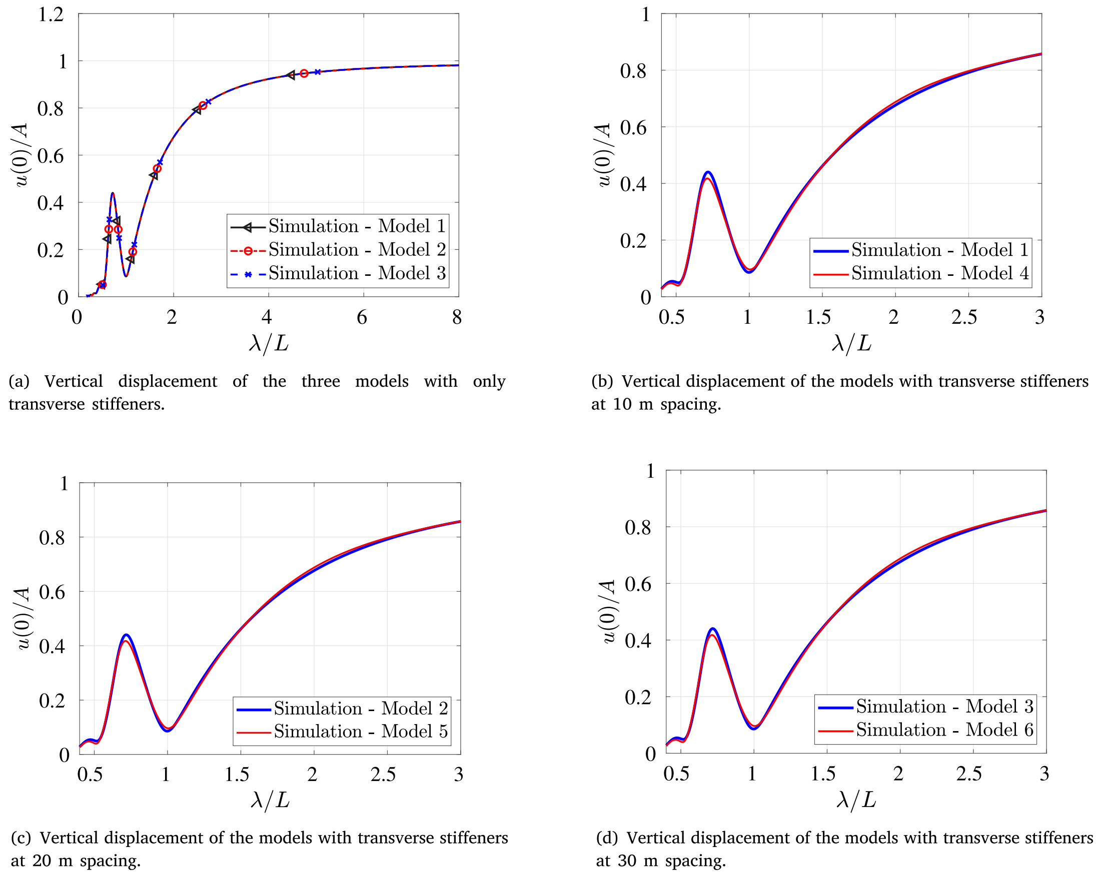

(a) Vertical displacement of the three models with only transverse stiffeners.

(b) Vertical displacement of the models with transverse stiffeners at 10 m spacing.

(c) Vertical displacement of the models with transverse stiffeners at 20 m spacing.

(d) Vertical displacement of the models with transverse stiffeners at 30 m spacing.

Fig. 20. Vertical displacement response at mid-ship section for various container ship models.

- STIFF' denotes calculations using the program STIFF [60], and 'Senjanovic - FEM' denotes results from a full FEM model. The average value of the FEM results [59] is indicated by the horizontal blue line computed from

$$\psi_{avg.} = \frac{1}{L}\int_0^L \psi(x)dx, \tag{49}$$

where $\psi(x)$ is either I_y, or I_z. Although the engine room near $x = 90$ m introduces some nonlinear variation into the sectional properties, they can be reasonably well approximated by the red lines labeled 'Simplified' in the plots. This line is obtained by using the NIAH approximation over the parallel mid-body, which in this case runs from about $x = 99$ m to $x = 224$ m, and then drawing straight lines from there to the bow and stern values. For the vertical and transverse area moment of inertia, the bow and stern values can be estimated from an FEM or other method. The error in the average value using the simplified method for this example is less than 1.35%. This illustrates how the suggested method can be easily applied to the practical analysis of large modern ships.

6. Conclusions

In the hydroelastic analysis of flexible structures, an accurate estimate of the structural stiffness is key for the correct prediction of the motion response to wave loads. However, for modern ships, the complexity of the cross section, and the large difference in scales between the local hull-girder elements and the length of the ship makes it challenging to accurately calculate the structural stiffness. Since modern large ship hulls are generally nearly periodic along much of their length, with a nearly-linear behavior towards the ends, we have introduced a novel implementation of asymptotic homogenization (NIAH) to efficiently calculate the structural stiffness which can greatly improve the computational efficiency. This implementation of NIAH is combined with a linearized potential flow hydrodynamic solver to provide efficient estimates of the hydroelastic response of ships. The effectiveness of the proposed workflow has been validated through several examples using both solid-section and thin-walled models.

Considering the structural configuration of real ships, we also use the new workflow to study the hydroelastic response of several representative open-section models of a container ship. The calculation of the structural stiffness using NIAH has been shown to be rapidly convergent with unit-cell size. The influence of both transverse and longitudinal stiffeners on the motion response was

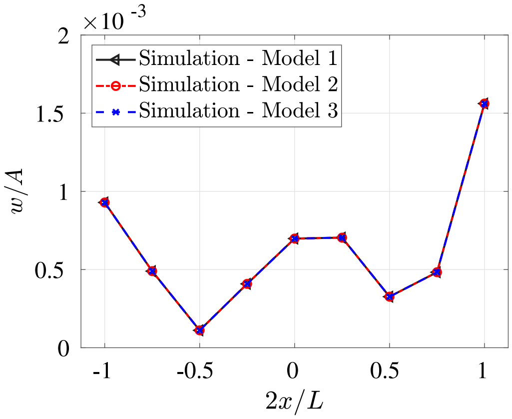

(a) Vertical deformation of the three models with only transverse stiffeners.

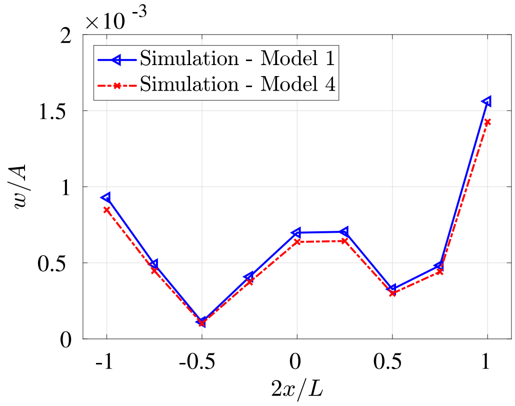

(b) Vertical deformation of the models with transverse stiffeners at 10 m spacing.

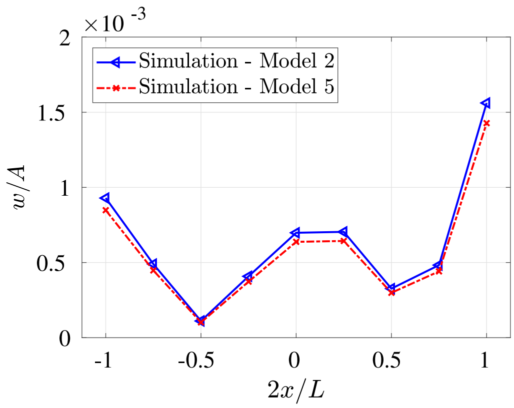

(c) Vertical deformation of the models with transverse stiffeners at 20 m spacing.

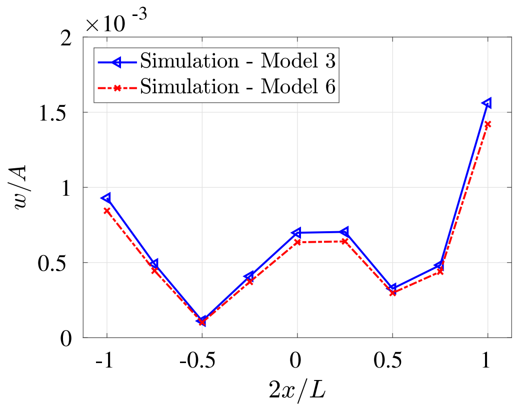

(d) Vertical deformation of the models with transverse stiffeners at 30 m spacing.

Fig. 21. Vertical deformation along a container ship in waves with λ/L = 0.714864.

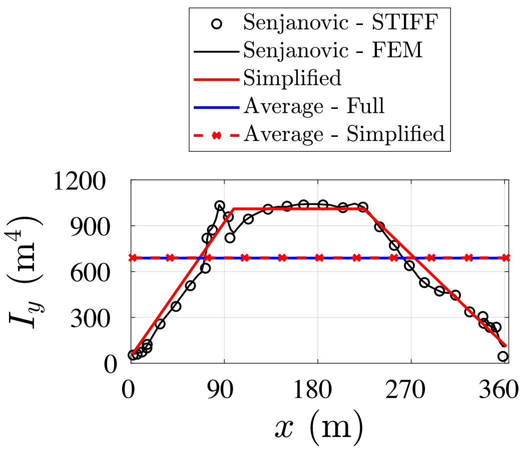

(a) Vertical area moment of inertia.

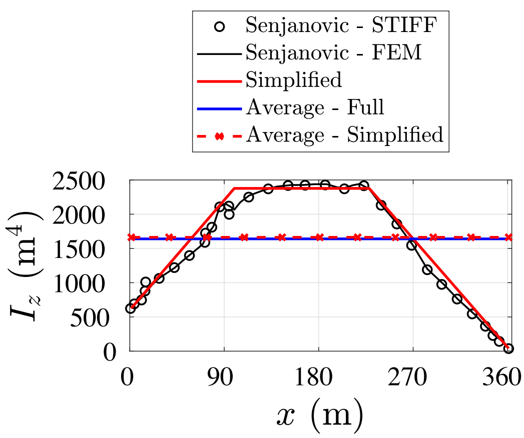

(b) Transverse area moment of inertia.

Fig. 22. Longitudinal distribution of ship cross-section geometrical properties [59].

studied for a representative large container ship model. These calculations illustrate how longitudinal stiffeners mainly influence the bending stiffness while transverse stiffeners mainly change the torsional stiffness, which can provide guidance for the proper design of the hull girder. A simple method for including the end effects was also proposed and demonstrated to give very small errors using a real container ship.

In this work, the hull girder has been treated as a uniform Euler–Bernoulli beam, so shear effects have been neglected. Work is however in progress to include sheer effects by treating the ship as a Timoshenko beam. The implementation of hydroelastic solutions including both shear and torsional modes will be presented in a future publication.

Declaration of competing interest

The authors declare that they have no known competing financial interests or personal relationships that could have appeared to influence the work reported in this paper.

Data availability

Data will be made available on request.

Acknowledgments

First author Baoshun Zhou is funded by China Scholarship Council (NO. 202006060053). Mostafa Amini-Afshar and Harry B. Bingham are very grateful to Den Danske Maritime Fond and Orients Fond for their financial support. This work has been carried out at Department of Civil and Mechanical Engineering, Section for Fluid Mechanics, Coastal and Maritime Engineering.

References

[1] Wu Y, Wang D, Riggs HR, Ertekin RC. Composite singularity distribution method with application to hydroelasticity. Mar Struct 1993;6(2–3):143–63.
[2] Kim KH, Bang JS, Kim JH, Kim Y, Kim SJ, Kim Y. Fully coupled BEM-FEM analysis for ship hydroelasticity in waves. Mar Struct 2013;33:71–99.
[3] Cheng Y, Ji C, Zhai G, Gaidai O. Hydroelastic analysis of oblique irregular waves with a pontoon-type VLFS edged with dual inclined perforated plates. Mar Struct 2016;49:31–57.
[4] Karperaki A, Belibassakis K, Papathanasiou T. Time-domain, shallow-water hydroelastic analysis of VLFS elastically connected to the seabed. Mar Struct 2016;48:33–51.
[5] Ding J, Tian C, Wu Y, Li Z, Ling H, Ma X. Hydroelastic analysis and model tests of a single module VLFS deployed near islands and reefs. Ocean Eng 2017;144:224–34.
[6] Cheng Y, Ji C, Zhai G, Oleg G. Fully nonlinear numerical investigation on hydroelastic responses of floating elastic plate over variable depth sea-bottom. Mar Struct 2017;55:37–61.
[7] Iijima K, Yao T, Moan T. Structural response of a ship in severe seas considering global hydroelastic vibrations. Mar Struct 2008;21(4):420–45.
[8] Wei W, Fu S, Moan T, Song C, Ren T. A time-domain method for hydroelasticity of very large floating structures in inhomogeneous sea conditions. Mar Struct 2018;57:180–92.
[9] Yang P, Li Z, Wu Y, Wen W, Ding J, Zhang Z. Boussinesq-Hydroelasticity coupled model to investigate hydroelastic responses and connector loads of an eight-module VLFS near islands in time domain. Ocean Eng 2019;190:106418.
[10] Kim SJ, Jin C, Lee I, Kim GJ, Kim M, Kwak HG. Efficient time-domain approach for hydroelastic-structural analysis including hydrodynamic pressure distribution on a moored SFT. Mar Struct 2023;90:103402.
[11] Bauchau OA, Craig JI. Euler-Bernoulli beam theory. In: Structural analysis, vol. 163. Springer; 2009, p. 173–221.
[12] Civalek Ö, Demir Ç. Bending analysis of microtubules using nonlocal Euler–Bernoulli beam theory. Appl Math Model 2011;35(5):2053–67.
[13] Masashi K, Shintaro K, Susumu C. Time- and frequency-domain calculation methods for ship hydroelasticity with forward speed. In: Proceedings of the 7th international conference on hydroelasicity in marine technology. 2015, p. 477–92.
[14] Timoshenko SP. On the transverse vibration of bars of uniform cross-section. Lond Edinb Dublin Philos Mag J Sci 1922;43(253):125–31.
[15] Timoshenko SP. On the correction for shear of the differential equation for transverse vibrations of prismatic bars. Lond Edinb Dublin Philos Mag J Sci 1921;41(245):744–6.
[16] Greenshields CJ. OpenFOAM user guide version 6. The OpenFOAM Foundation Ltd; 2018.
[17] Cd-Adapco S. STAR CCM+ user guide version 12.04, vol. 62. New York, USA: CD-Adapco; 2017.
[18] Newman JN, Lee C-H, Korsmeyer FT. WAMIT: a radiation-diffraction panel program for wave-body interactions. Chestnut Hill, MA, USA; 2014, http://www.wamit.com.
[19] Lee CH. WAMIT theory manual. Massachusetts Institute of Technology, Department of Ocean Engineering; 1995.
[20] Newman JN. Efficient hydrodynamic analysis of very large floating structures. Mar Struct 2005;18(2):169–80.
[21] Chen XB. Hydrostar for experts user manual. Paris: Bureau Veritas; 2010.
[22] Malenica Š, Derbanne Q. Hydro-structural issues in the design of ultra large container ships. Int J Nav Archit Ocean Eng 2014;6(4):983–99.
[23] Newman JN. Wave effects on deformable bodies. Appl Ocean Res 1994;16(1):47–59.
[24] Amini-Afshar M, Bingham HB. Solving the linearized forward-speed radiation problem using a high-order finite difference method on overlapping grids. Appl Ocean Res 2017;69:220–44.
[25] Amini-Afshar M, Bingham HB. Pseudo-impulsive solutions of the forward-speed diffraction problem using a high-order finite-difference method. Appl Ocean Res 2018;80:197–219.
[26] Amini-Afshar M, Bingham HB, Henshaw WD. Stability analysis of high-order finite-difference discretizations of the linearized forward-speed seakeeping problem. Appl Ocean Res 2019;92:101913.
[27] Andersen MH, Amini-Afshar M, Bingham HB. Implementation of generalized modes in a 3D finite difference based seakeeping model. In: Proceedings of the 32nd international workshop on water waves and floating bodies. 2017, p. 4.
[28] Zhou B, Amini-Afshar M, Bingham HB, Shao Y. Hydroelastic solutions using a high-order finite difference method on overlapping grids. In: Proceedings of 9th international conference on hydroelasticity in marine technology. 2022, p. 9.

[29] Zhou B, Amini-Afshar M, Bingham HB, Shao Y. Hydroelastic solutions using a high-order finite difference method based on the mode functions of a timoshenko beam. In: 23rd nordic maritime universities workshop. 2023, p. 1.
[30] Field E, Herting D, Morgan M. NASTRAN user's guide (Level 17.5). NASA; 1979.
[31] Abaqus G. ABAQUS 6.11. Providence, RI, USA: Dassault Systemes Simulia Corporation; 2011.
[32] Madenci E, Guven I. The finite element method and applications in engineering using ANSYS®. Springer; 2015.
[33] Kanit T, Forest S, Galliet I, Mounoury V, Jeulin D. Determination of the size of the representative volume element for random composites: statistical and numerical approach. Int J Solids Struct 2003;40(13–14):3647–79.
[34] Hassani B, Hinton E. A review of homogenization and topology optimization I—homogenization theory for media with periodic structure. Comput Struct 1998;69(6):707–17.
[35] Hassani B, Hinton E. A review of homogenization and topology opimization II—analytical and numerical solution of homogenization equations. Comput Struct 1998;69(6):719–38.
[36] Yi S, Xu L, Cheng G, Cai Y. FEM formulation of homogenization method for effective properties of periodic heterogeneous beam and size effect of basic cell in thickness direction. Comput Struct 2015;156:1–11.
[37] Bensoussan A, Lions J-L, Papanicolaou G. Asymptotic analysis for periodic structures, vol. 374. American Mathematical Soc.; 2011.
[38] Sanchez-Palencia E. Homogenization method for the study of composite media. In: Asymptotic analysis II— surveys and new trends. Springer; 2006, p. 192–214.
[39] Bakhvalov NS, Panasenko G. Homogenisation: averaging processes in periodic media: mathematical problems in the mechanics of composite materials, vol. 36. Springer Science & Business Media; 2012.
[40] Daya EM, Braikat B, Damil N, Potier-Ferry M. Continuum modeling for the modulated vibration modes of large repetitive structures. C R Méc 2002;330(5):333–8.
[41] Daya EM, Jeblaoui K, Potier-Ferry M. A two scale method for modulated vibration modes of large, nearly repetitive, structures. C R Méc 2003;331(6):443–8.
[42] Daya EM, Braikat B, Damil N, Potier-Ferry M. Modelisation of modulated vibration modes of repetitive structures. J Comput Appl Math 2004;168(1–2):117–24.
[43] Kolpakov AG. Variational principles for stiffnesses of a non-homogeneous beam. J Mech Phys Solids 1998;46(6):1039–53.
[44] Kolpakov AG. Stressed composite structures: homogenized models for thin-walled nonhomogeneous structures with initial stresses. Springer Science & Business Media; 2004.
[45] Buannic N, Cartraud P. Higher-order effective modeling of periodic heterogeneous beams. I. Asymptotic expansion method. Int J Solids Struct 2001;38(40–41):7139–61.
[46] Buannic N, Cartraud P. Higher-order effective modeling of periodic heterogeneous beams. II. Derivation of the proper boundary conditions for the interior asymptotic solution. Int J Solids Struct 2001;38(40–41):7163–80.
[47] Kim JS, Wang K. Vibration analysis of composite beams with end effects via the formal asymptotic method. J Vib Acoust 2010;132(4).
[48] Kolpakov A. Calculation of the characteristics of thin elastic rods with a periodic structure. J Appl Math Mech 1991;55(3):358–65.
[49] Cheng G, Cai Y, Xu L. Novel implementation of homogenization method to predict effective properties of periodic materials. Acta Mech Sin 2013;29(4):550–6.
[50] Cai Y, Xu L, Cheng G. Novel numerical implementation of asymptotic homogenization method for periodic plate structures. Int J Solids Struct 2014;51(1):284–92.
[51] Xu L, Cheng G, Yi S. A new method of shear stiffness prediction of periodic Timoshenko beams. Mech Adv Mater Struct 2016;23(6):670–80.
[52] Xu L, Cheng G. Shear stiffness prediction of Reissner–Mindlin plates with periodic microstructures. Mech Adv Mater Struct 2017;24(4):271–86.
[53] Yan J, Hu H, Yang Z, Wan R, Li Y. Multi-scale analysis for helically wound structures with one-dimensional periodicity. Eng Comput 2019;36(8):2911–28.
[54] Yan J, Zhou B, Yang Z, Xu L, Hu H. Mechanism exploration and effective analysis method of shear effect of helically wound structures. Finite Elem Anal Des 2022;212:103840.
[55] Gere JM, Goodno BJ. Mechanics of materials. Cengage Learning; 2012.
[56] Malenica Š. Hydroelastic response of a barge to impulsive and non-impulsive wave loads. In: Proceedings of the 3rd international conference on hydroelasticity in marine technology. 2003, p. 107–15.
[57] Young W, Roark R, Budynas R. Roark's formulas for stress and strain. McGraw-Hill Eudcation; 2002, Available from: https://books.google.dk/books?id=BnxUAAAAMAAJ.
[58] Dizy J, Palacios R, Pinho ST. Homogenisation of slender periodic composite structures. Int J Solids Struct 2013;50(9):1473–81.
[59] Senjanović I, Tomašević S, Vladimir N. An advanced theory of thin-walled girders with application to ship vibrations. Mar Struct 2009;22(3):387–437.
[60] Fan Y, Senjanović I. STIFF, user's manual. Zagreb: Faculty of Mechanical Engineering and Naval Architecture; 1990, p. 1–49.